2013

Aerodynamic Measurements of a Variable-Speed Power-Turbine Blade Section in a Transonic Turbine Cascade

Ashlie B. Flegel
Cleveland State University

AERODYNAMIC MEASUREMENTS OF A VARIABLE-SPEED POWER-TURBINE BLADE SECTION IN A TRANSONIC TURBINE CASCADE

ASHLIE B. FLEGEL

Bachelor of Science in Mechanical Engineering

The University of Toledo

May 2007

Submitted in partial fulfillment of requirement for the degree

MASTER OF SCIENCE IN MECHANICAL ENGINEERING

at the

CLEVELAND STATE UNIVERSITY

DECEMBER 2013

We hereby approve this thesis of

Ashlie B. Flegel

Candidate for the Master of Science in Mechanical Engineering degree for the

Department of Mechanical Engineering

and the CLEVELAND STATE UNIVERSITY

College of graduate Studies

_____

Thesis Committee Chairperson, Dr. Mounir Ibrahim

_____

Department/ Date

_____

Dr. Ralph Volino

_____

Department/ Date

_____

Dr. Miron Kaufman

_____

Department/ Date

Student's Date of Defense: 12/05/2014

ACKNOWLEDGEMENTS

I would first like to thank my thesis advisor, Dr. Mounir Ibrahim, for his support and encouragement. I also wish to thank my research group members Dr. Paul Giel of Vantage Partners, LLC and Dr. Gerard Welch of NASA Glenn Research Center for their support and guidance throughout this research effort. This thesis would not be possible without them. This work is supported under the NASA Fundamental Aeronautics Program, Rotary Wing Project. I'd like to thank my family members for all of their support and motivation.

AERODYNAMIC MEASUREMENTS OF A VARIABLE-SPEED POWER-TURBINE BLADE SECTION IN A TRANSONIC TURBINE CASCADE

ASHLIE B. FLEGEL

ABSTRACT

The purpose of this thesis is to document the impact of incidence angle and Reynolds number variations on the 3-D flow field and midspan loss and turning of a 2-D section of a variable-speed power-turbine (VSPT) rotor blade. Aerodynamic measurements were obtained in a transonic linear cascade at NASA Glenn Research Center in Cleveland, OH. Steady-state data were obtained for ten incidence angles ranging from +15.8° to −51.0°. At each angle, data were acquired at five flow conditions with the exit Reynolds number (based on axial chord) varying over an order-of-magnitude from 2.12×10^5 to 2.12×10^6. Data were obtained at the design exit Mach number of 0.72 and at a reduced exit Mach number of 0.35 as required to achieve the lowest Reynolds number. Midspan total-pressure and exit flow angle data were acquired using a five-hole pitch/yaw probe surveyed on a plane located 7.0 percent axial-chord downstream of the blade trailing edge plane. The survey spanned three blade passages. Additionally, three-dimensional half-span flow fields were examined with additional probe survey data acquired at 26 span locations for two key incidence angles of +5.8° and −36.7°. Survey data near the endwall were acquired with a three-hole boundary-layer probe. The data were integrated to determine average exit total-pressure and flow angle as functions of incidence and flow conditions. The data set also includes blade static pressures measured on four spanwise planes and endwall static pressures.

TABLE OF CONTENTS

LIST OF TABLES

LIST OF FIGURES

NOMENCLATURE

Cp_s	static pressure coefficient, $Cp_s=(P-\bar{P}_2)/(P_{t,1}-\bar{P}_2)$
Cp_t	total-pressure coefficient, $Cp_t=(P_{t,1}-P_t)/(P_{t,1}-\bar{P}_2)$
C_x	blade axial chord [in]
H	blade span [in]
i	incidence angle, $i = \beta_1$ – inlet metal angle (34.2°)
M	Mach number
N	power-turbine shaft speed [rpm]
N^*	$N/N_{100\%}$, fraction of 100% speed
PR	pressure ratio, $PR = P_{t,1}/\bar{P}_2$
PS	pressure surface
$\bar{P}$	area-averaged static-pressure
P_s	static pressure
P_t	total pressure
$\bar{P}_t$	area-averaged total-pressure
Re	Reynolds number, $Re = \rho_2 U_2 C_x/\mu$
Re_b	baseline exit Reynolds number, $Re_b = 5.30\times10^5$
S	blade pitch [in]
SS	suction surface
Tu	turbulence intensity, $Tu = \sqrt{u_s^2}/U$
U	total mean velocity [ft/s]
$\underline{U}$	mean velocity [ft/s], $\underline{U} = (U_x, U_y, U_z)$
$\underline{u}$	fluctuating velocity, $\underline{u} = (u_x, u_y, u_z)$

x	chordwise (axial) coordinate [in]
y	pitchwise (tangential) coordinate [in]
z	spanwise coordinate [in]
Zw	Zweifel coefficient, Zw $=\frac{2S}{C_x}cos^2\bar{\beta}_2\left(tan\beta_1 - tan\bar{\beta}_2\right)$
β	relative flow angle, pitch angle [deg.], $\beta = \tan^{-1}(U_y / U_x)$
$\bar{\beta}_2$	angle of mass-averaged velocity components
$\Delta\beta_2$	departure angle from trailing edge mean camber line
γ	yaw angle [deg.], $\gamma = \tan^{-1}(U_z / U_x)$
δ_1	boundary-layer displacement thickness [in.]
δ_2	momentum thickness [in.]
δ_{99}	boundary layer thickness [in.]
μ	dynamic viscosity
ρ	density
τ	probe time constant [s]
ω	loss coefficient, $\omega = \left(P_{t,1} - \bar{P}_t\right)/\left(P_{t,1} - \bar{P}_2\right)$
ω_c	loss coefficient, $\omega_c = \omega\ (Re/Re_b)^{1/2}$

Subscripts

1	cascade inlet value
2	cascade exit value
i	isentropic value
s	streamwise component
t	total condition

CHAPTER I

INTRODUCTION

The aerodynamic effects of large incidence and Reynolds number variations on a 2-D midspan section of a variable speed power turbine (VSPT) blade are investigated in this study. Downstream midspan total-pressure, exit flow angles, and blade loading measurements were acquired for ten incidence angles and at five flow conditions each. This dataset is important for understanding the aerodynamic challenges of a VSPT application for a Large-Civil Tilt-Rotor (LCTR). Detailed 3-D half-span flowfield measurements were acquired for two incidence angles corresponding to the LCTR points of cruise and takeoff. Because admitting transitional flow on the blade surface was of importance for this study, all the tests were conducted with low inlet turbulence.

In this chapter, the motivation behind a VSPT will be discussed. The VSPT is a key driver in allowing efficient operation of a LCTR. The VSPT will allow the main rotor speeds to vary from 100% at takeoff to 54% at cruise. At these large speed variations, incidence angle and Reynolds number effects are important. In a review of the literature it will be discovered that little experimental data exists that covers a large applicable

range of incidence angles at engine relevant Reynolds and Mach numbers. The chapter will conclude with discussion of the scope of this thesis.

Motivation

The Rotary Wing Project of the NASA Fundamental Aeronautics Program is investing in technology to enable civil rotor craft use to help relieve airport congestion and enhance airspace throughput capacity. One concept vehicle of interest is the Large Civil Tilt-Rotor (LCTR). The LCTR is an economically competitive rotary-wing vehicle with both VTOL and Mach 0.5 cruise capability (Johnson et al. [1] and Acree et al. [2]). In order to minimize mission fuel burn, it has been found that the main rotor speeds must vary from 100% N^* at takeoff to 54% N^* at cruise in order to optimize the propulsive efficiency at cruise. In order to accommodate this large speed variation, a variable gear-ratio (two-speed) transmission can be used (Stevens et al. [3]), which introduces complexities such as gear shifting during flight and additional weight of the transmission. Another approach is to use a variable speed power turbine (VSPT) (D'Angelo [4] and Welch [5]).

There are several challenges associated with the VSPT technology which include attainment of high turbine efficiency at high work factors, management of loss levels over a large (40°-60°) incidence variation in all blade rows, and operation at low Reynolds numbers (transitional flow) (Welch [5]). Understanding the loss levels due to incidence and effects of transitional flow are the two challenges which are the focus of this thesis. These challenges stem from the consideration of two key LCTR mission points: 2,000 ft takeoff/hover and 28,000 ft Mach 0.5 cruise. At takeoff, the main rotor

and VSPT operate at 100% *N**, while at cruise the rotors and VSPT are slowed to 54% N*. The engine requirements for an LCTR were established in a previous study [6]. In that study, it was found that as the main rotor shaft is reduced by nearly 54% from take-off to cruise speed the corrected flows do not change significantly and the flow coefficient essentially doubles. The nearly constant corrected flow rates and 40% corrected speed change lead to incidence angle swings of 40° and 60° in all turbine blade and vane rows downstream of the first vane, including any required exit guide vane row. The study also indicated that the unit Reynolds numbers (in^{-1}) at the aft-stage rotor exit of the VSPT for the LCTR application varies between $0.45\times10^5<Re/C_x$ $[in^{-1}] < 0.75\times10^5$ from takeoff to cruise. This is a range in which transitional flow may impact performance.

Literature Review

Several studies have been reported in the literature that address challenges relevant to variable-speed power turbines. With respect to the Reynolds number effects on the blade losses, this has been well documented in the open literature for Low Pressure Turbine (LPT) applications. Hourmouziadis [7], Haselbach [8], and Gier et al. [9] considered the impact of Reynolds number lapse on LPT blade row performance. Halstead et al. [10] and Coull et al. [11] addressed the sensitivity of the transitional flow fields to deterministic unsteadiness associated with upstream wakes. This thesis does not explore the impact of wake passing on blade row performance. All tests were carried out in a steady-state cascade.

The effects of a wide range incidence on blade loading and downstream wakes for a wide range of engine relevant flow conditions are scarce in the open literature. Some studies addressing incidence effects will now be discussed. Yamamoto and Nousse [12] conducted exhaustive tests in a low speed cascade looking at the impact of incidence on the 3-D flow field and losses over a 60.5° incidence range ($-53.3° < i < +7.2°$)for five discrete angle settings. Five-hole pressure probe surveys were conducted on 15-16 axial planes downstream and upstream of the blade row and between blade passages from hub to midspan. This study only examined the incidence effects at one Reynolds number condition. The authors noted that Reynolds number will influence the boundary layer thicknesses at the inlet endwall and blade surface. There will also be changes in the turbulence level as the velocity is varied. In Yamamoto and Nousse's [12] study, the chordwise development of the secondary flows and total-pressure fields were provided for the five incidence angles tested. The authors noted that the front part of the blade is very sensitive to incidence and that the front loading decreases with decreasing incidence. The total pressure contours indicate two loss regions, one located on the suction surface where it is insensitive to incidence and on the pressure surface near the leading edge which increases with increasing negative incidence. The authors observed the endwall effects related to incidence and found that as incidence increases; the flow migrates towards the suction surface. This is consistent with Hodson and Dominy's [13] findings which show the low momentum endwall flow accumulating on the blade suction surface. The losses due to the suction side and pressure side leg of the horseshoe vortex and passage vortex was observed. The intersection of the horseshoe and passage vortex moves from suction to pressure side as the incidence increases. The cascade incidence

influences the passage vortex and horseshoe vortex intersection which rotates in the same direction.

Moustapha et al. [14] have summarized previous work related to profile and secondary flow losses at design and off-design incidence conditions. In addition to Moustapha et al.'s [14] valuable review of available cascade data with wide ranges of incidence angle testing, they noted that blade rows with high inlet Mach numbers would likely be more sensitive to inlet gas angle changes. They also noted the lack of data in the open literature related to the impact of compressibility, leading edge geometry, and axial loading schedule on incidence losses.

Joinini et al. [15] examined the impact of leading edge geometry—in particular, metal angle selection—on midspan incidence loss. They noted that detailed experimental data for off-design incidence, particularly in transonic flow conditions, were sparse in the open literature, and highlighted the importance of such data for CFD validation.

Turbulence effects play a role in the losses of a turbine cascade as examined in Hoheisel et al. [16]. Measurements were made on three blade geometries; one was front-loaded and two were aft-loaded blading. Tests were conducted in a seven blade linear cascade. The authors noted that it is the boundary layer transition that determines the losses on turbine cascades. It is essential to have velocity distributions with the laminar-turbulence transition point as far downstream as possible. The two factors affecting transition behavior are the pressure gradient on the blade surface and the free stream turbulence levels. The laminar separation bubble influenced the boundary layer transition; its size was reduced with increasing Reynolds number and turbulence. The aft-loaded blading performed better in terms of loss at the different incidence levels at Tu =

5%. The most front-loaded blade performed more poorly at positive incidence but retained lower loss levels at negative incidence.

Corriveau and Sjolander [17] provided midspan profile losses, loading distributions, and base pressure measurements for a series of HPT airfoils with front-, mid-, and aft-loading. The linear cascade tests were conducted over a wide range of LPT-relevant Mach numbers and at Reynolds numbers from 0.4 to 1.0×10^6. While the results illustrated superior loss performance for aft-loaded blades, lower loss levels were achieved at off-design incidence with the mid-loaded blading.

Scope of Work

The objective of this thesis is to advance the understanding of the aerodynamic effects of large incidence angle and Reynolds number variations with the development of an extensive cascade dataset that addresses the key VSPT challenges. The NASA Transonic Linear Cascade Facility was used to assess the performance of a VSPT blade section at design and off-design inlet flow angles over an engine-relevant range of Mach and Reynolds numbers.

Chapter II contains descriptions of the experimental facility and of the instrumentation used during this study. While the facility boasts many capabilities that made it desirable to test the VSPT blade geometry, modifications had to be made in order to span the desired incidence range. After discussing the facility, a description of the instrumentation will be given. This will highlight the features of obtaining measurements of the inlet boundary layer, inlet turbulence, and exit flow features.

In Chapter III a description of the current experiment will be given. The 2-D extruded midspan section of the VSPT blade geometry will be described. This chapter will also discuss the test configuration and the test matrix.

Chapter IV will present the results of the aerodynamic measurements acquired for ten incidence angles at five flow conditions. The chapter will begin with looking at the three-dimensional flowfield measurements for the take-off (i = −36.7°) and cruise (i= +5.8°) angles. These data, along with the blade loadings, will show the influence of secondary flows on the blade loading. Pitchwise integrated averages of the half-span data are shown as well. The 2-D midspan total-pressure and exit pitch angle measurements for all ten incidence angles varying from i = +15.8° to i= −51.0° will then be presented. Averaged midspan total pressures were used to establish profile loss buckets.

Chapter V will conclude with a summary of the major findings and recommendations for future research.

CHAPTER II

EXPERIMENTAL FACILITY

The experimental study was conducted at NASA Glenn Research Center's (GRC) Transonic Turbine Blade Cascade Facility. This large-scale linear cascade facility was desirable for this test because of its adjustable inlet flow angle test section (77° range), wide range of flow (Mach and Reynolds number) capabilities, the large-scale blades which enable detailed flow field measurements, and the large number of blades which would promote better periodicity. Testing in the steady-state, non-rotating cascade inherently neglects the rotational effects associated with Coriolis and centrifugal acceleration fields, the relative motion of endwalls, and the impact of unsteadiness of upstream and downstream blade rows. However, a transonic cascade test of a VSPT blade section will allow for the examination of the fundamental physics occurring and will serve as an important step towards VSPT technology level advancement.

Facility Description

The NASA GRC Transonic Turbine Blade Cascade Facility is shown in Fig. 1. A detailed facility description is given in Verhoff et al. [18]. Since then, the inlet flow boards were modified to improve the inlet flow uniformity as described in Giel et al. [19]. The cascade's large scale and continuous run capability at engine relevant Mach numbers and Reynolds numbers have allowed for detailed aerodynamic [20, 21] and heat transfer studies [22, 23] on a wide range of turbine blades.

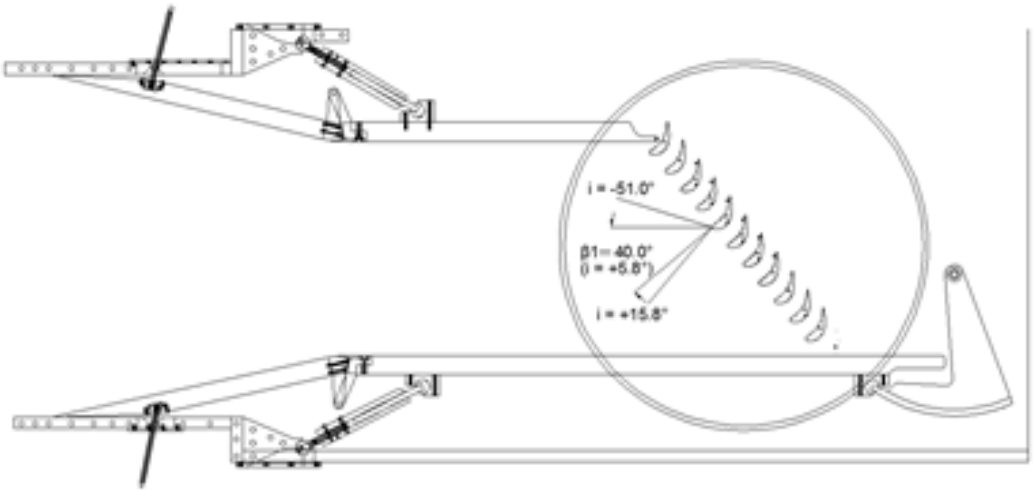

Figure 1. Cascade Test Section with Blade Geometry.

The tunnel operates by utilizing inlet air that is supplied by GRC's 40 psig Combustion Air system. Clean, dry, ambient temperature air enters the facility and is throttled to a maximum inlet pressure of 14.7 psia under current safety restrictions. This restriction is shown as the red dashed line in Fig. 2. The air passes through flow conditioning and contraction sections and is directed to the cascade test section by upper and lower inlet flow boards. The air is then exhausted through an altitude exhaust system

that is maintained at 2 psia. Independent control of the inlet and exhaust valves allows for a wide range of engine relevant Mach and Reynolds numbers to be achieved, as shown in the facility operating envelope of Fig. 2.

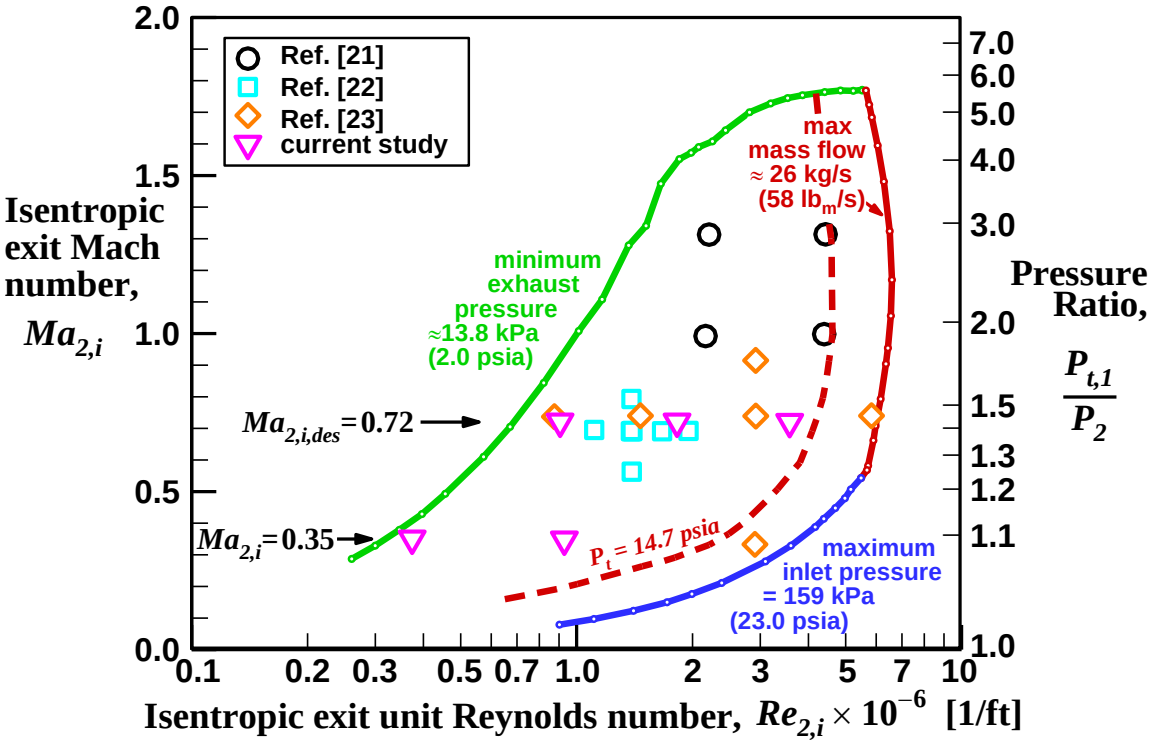

Figure 2. Operating Envelope of NASA Transonic Turbine Cascade.

For this study, the cascade was made up of nominally ten blade passages. The blades are attached to a disk that can be rotated to set inlet flow angles (from axial) in the range $-17° \leq \beta_1 \leq +78.8°$. This allows for a wide range (96°) of incidence angles to be studied. Prior to this test the original facility configuration (see Fig. 3) allowed a 45° range in inlet angles from $+33.8° \leq \beta_1 \leq +78.6°$. These angles are typical of HPT (high pressure turbine) applications. In the previous chapter it was noted that the VSPT may

see incidence swings of 40° to 60°. The blade designs also require lower inlet flow turning for more negative incidence. This VSPT requirement resulted in modifications to cascade's exhaust and inlet board configurations as described by McVetta et al. [20]. The modifications, shown in Fig. 4, include a new exhaust which extends the length of the top of the tunnel and structural supports in the test section in order to accommodate the range of the exit angles required for the current tests. As part of the facility modifications, unique upper flow board extensions with respective blade suction-side profiling were fabricated for five discrete incidence angles in the range of $-16.1° \leq i \leq -51.0°$. For these five angles, the upper-most blade was removed and replaced with a flow board extension that connected at the blade bolt hole and to the end of the original upper flow board. These extensions ensured that the flow was properly directed into the first blade passage, the upper and lower flow boards were horizontal, and the flow board hinged leading edges were maintained in the same plane normal to the inlet flow. The other incidence angles tested outside of this range did not require an upper extension board and utilized the original flow board configuration.

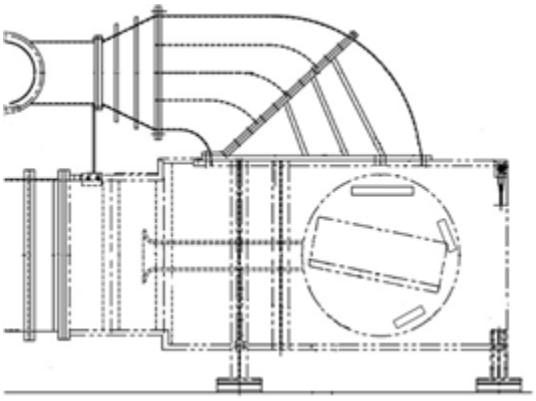

Figure 3. Original Facility Configuration.

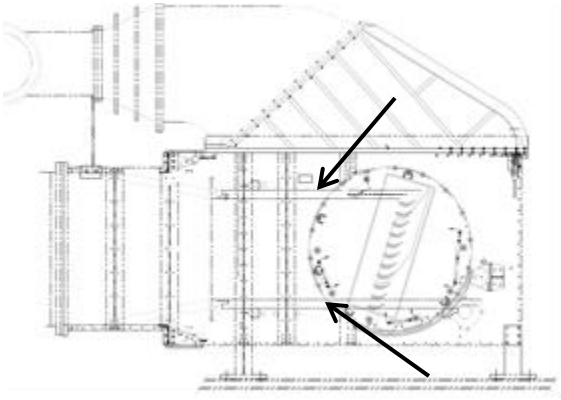

Figure 4. Facility After Modifications. Arrows indicate flow boards.

Instrumentation Description

Detailed data documenting the inlet characteristics and downstream flowfield along three blade passages were acquired by using pneumatic pressure probes, static taps, and a hotwire anemometer probe. Details of the instrumentation are discussed below.

Pressure Probes: Inlet boundary layer measurements and downstream total-pressure and exit flow angle data were acquired using a three-hole boundary layer probe and a five-hole pitch-yaw probe. The probes are shown in Figure 5. Both are 45° forward-facing pyramid probes with the measurement ports located on the shaft centerline. For the downstream aerodynamic measurements both probes were installed in a survey plane located 7.0% axial-chord downstream of the blade trailing edge in Station 2. The survey station locations are shown in Fig. 6 and cover three blade passages. Inlet boundary layers measurements were measured using the three-hole probe at Station 0, which is 0.415 axial-chords upstream of the blade leading edge. The boundary layer probe has a flattened probe end and can be traversed to touch the endwall and acquire measurements as close as 0.005 inches (0.13 mm) from the endwall surface.

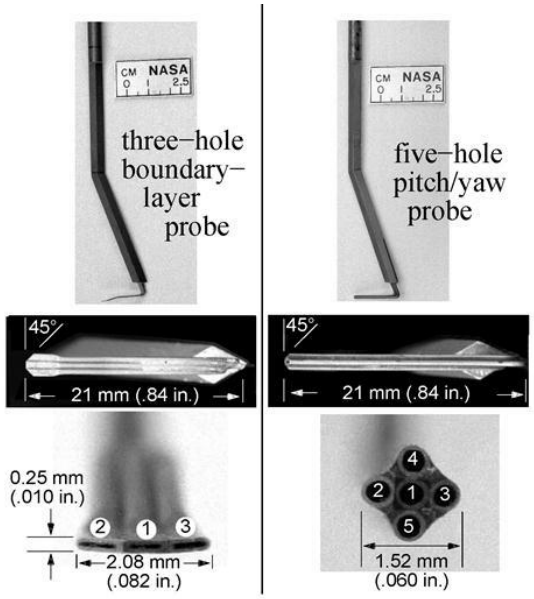

Figure 5. Three-Hole B-L Probe (left) and Five-Hole Probe Details.

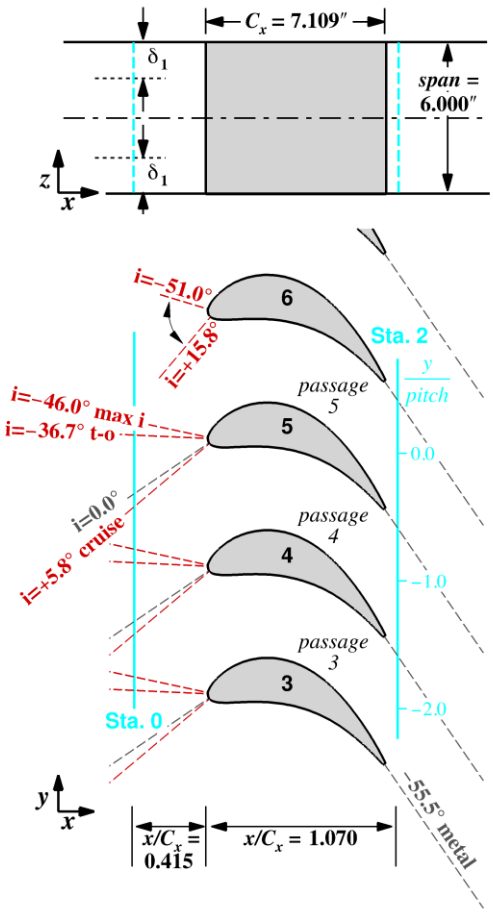

Figure 6. Blade Geometry and Survey Plane Locations.

The five-hole probe was used to measure total-pressure, pitch angle (*x*-*y* plane), and yaw angle (*x*-*z* plane). For each inlet angle, the five-hole probe was used for midspan surveys consisting of 123 pitchwise points spaced non-uniformly over the three passages noted in Figure 6. Pitchwise/spanwise surveys were also taken at the takeoff ($i = -36.7°$) and cruise ($i = +5.8°$) angles. The surveys at each immersion consisted of 62 pitchwise points spaced uniformly over three passages. The three-hole boundary-layer probe was used to measure total pressure and pitch angle only. The half-span 3-D flowfield was resolved by using the three-hole probe near the endwall for $0.0 < z/H \leq 0.043$ with 14 spanwise points spaced logarithmically. The five-hole probe was used above this region for $0.042 \leq z/H \leq 0.50$ with 12 spanwise points spaced uniformly.

Inlet boundary-layer measurements were acquired using the three-hole probe installed in Station 0, located 0.415 axial-chords upstream of the blades. The surveys were acquired at two to three pitch locations and consisted of 29 spanwise points.

Both pressure probes were calibrated using the same method as described in Giel et al. [21]. The probes were calibrated in NASA GRC's Free Jet Calibration Rig (CE-12). The pitch and yaw angles of the five-hole probe were calibrated over a Mach number range from 0.1 to 0.9. The pitch angle was traversed from ± 35° and the yaw ranged from ± 40°. Similarly, the three-hole probe was calibrated over the same Mach number and pitch angle range. During the cascade test, the probe pitch angle coefficient was monitored to ensure that it remained well within the angular calibration range corresponding to approximately ±40°. When needed, the probe survey was stopped and the probe was approximately nulled before resuming. The overall estimated uncertainty in flow angle was ±1.5° and the overall estimated local uncertainty in total-pressure

coefficient was ±1.7%, as reported in Giel et al. [21] and scaled for the current definition of total-pressure coefficient.

The time responses for each probe were measured to be: $\tau_{5\text{-hole}} = 0.42$s and $\tau_{3\text{-hole}} = 0.82$s. To ensure a 95% time recovery, a three second delay was imposed between the time the probe reaches the desired survey location and the initiation of data recording. Five readings, taken one second apart, were averaged at each measurement point.

Static Pressure Measurements: The primary measurement blades 4, 5, and 6, shown in Fig. 6, were instrumented with static pressure taps along four spanwise locations. Blade 5 was fully instrumented with 44 taps along 10%, 15%, 30%, and 50% of span. A pre-test RANS prediction of the blade surface pressure distribution, shown in Fig. 7, was used to establish the placement of the Blade 5 static taps. To verify periodicity, 20 redundant taps were installed on the suction side of Blade 4 and 16 taps were installed on the pressure side of Blade 6.

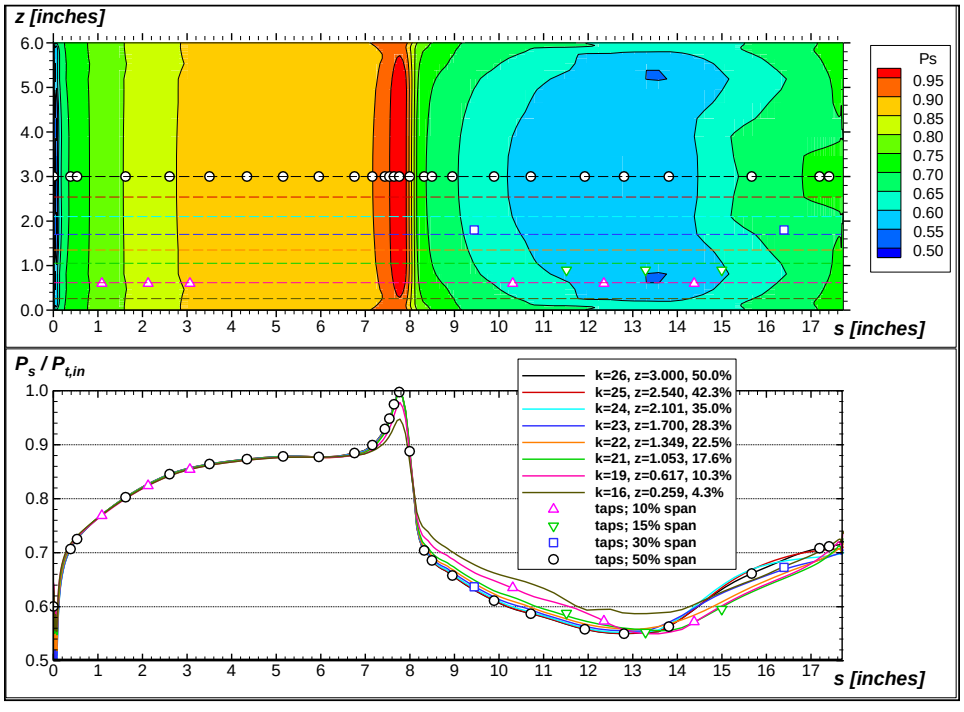

Figure 7. Blade Static Pressure Tap Locations.

The endwall was fully instrumented with approximately 550 static pressure taps located both upstream and downstream of the blade row and within each passage (see Figure 8). Data from these pressure measurements were used for periodicity checks which will be discussed in further detail in Chapter III.

Twelve exit static-pressure taps, located approximately three axial-chords downstream of the blades and spanning almost nine blade pitches, were used to set the exit Mach number condition. The inlet static pressure was measured by five to six inlet static pressure taps, depending on inlet flow angle, located 96.77 mm (3.81 inches) upstream of the blade row at Station 0. These inlet taps can be seen in Fig. 8, represented by the orange dots at $x = -5$ inches.

Additional inlet measurements: Inlet total pressure and temperature were measured with two combination Kiel/total-temperature probes located at midspan approximately 96.77 mm (3.81 inches) upstream of the blades, just outside the passages of interest. These Kiel probes, shown in Fig. 8 as the blue dots, were used to set the tunnel inlet conditions. A third Kiel probe was also used for some of the inlet flow angle measurements.

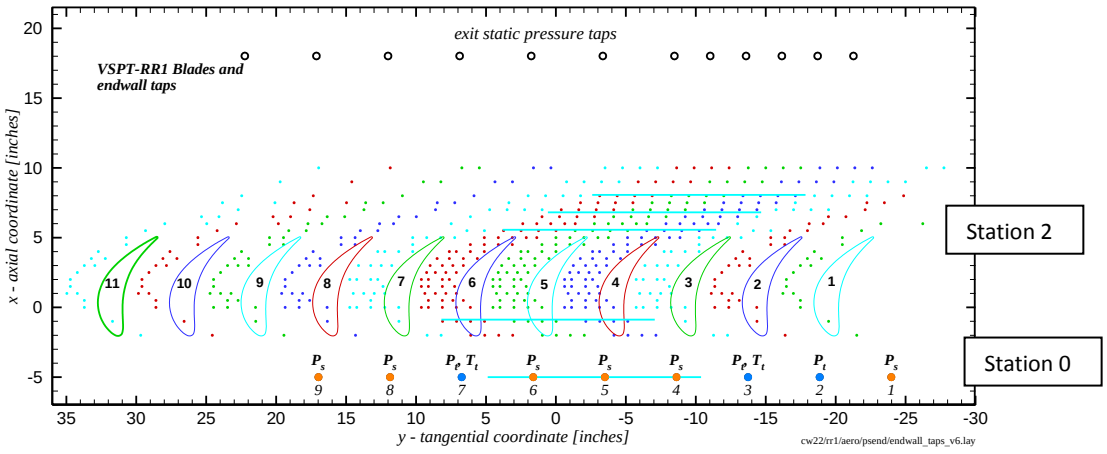

Figure 8. Endwall Instrumentation Configuration.

Hotwire Anemometer: A constant temperature single-wire hotwire anemometer probe (TSI 1210-T1.5) was used to acquire inlet turbulence intensity measurements. The hotwire was installed in Station 0, located approximately 0.415 axial chord upstream of the blades (see Fig. 8). The data were acquired at a rate of 92 kHz for 7 seconds. The uncertainties in the measurements were calculated to be less than 4% for the mean velocities and 5% for the fluctuations using the methodology found in [24]. The turbulence intensities, calculated as the normalized root-mean square of the velocity fluctuations, ranged from 0.25% to 0.40% [20]. The integral length scale was calculated though an autocorrelation technique (e.g., see Coull et al. [25]) and was found to be between 1.0 to 1.5 inches.

CHAPTER III

DESCRIPTION OF EXPERIMENT

Blade Description

The blade geometry is a scaled 2-D midspan section of the VSPT second stage rotor designed by Rolls-Royce. Details of the blade design are documented in [26]. In that effort, meanline analyses were used to analyze three and four-stage variable-speed power turbines (VSPT) to meet specified engine requirements. A 4-stage turbine was selected for additional optimization and a detailed 3-D blade aero design/optimization was concentrated on the second rotor of the selected 4-stage meanline design. Rotor 2 was selected as a representative embedded blade row, both in terms of turning (96° at cruise and 53^0 at takeoff) and incidence-range (42°) requirements between cruise and takeoff [26]. The midspan section, which was optimized to minimize loss at the cruise condition (i = +5.8°, $M_{2,i}$ = 0.72) and achieve the required incidence range at acceptable loss levels, was chosen for this cascade test. The blade has an inlet metal angle of 34.2° relative to the axial direction and a scaled axial chord of 180.6 mm (7.109 in). Details of the scaled (test) blade are listed in Table I. The cascade of the current test comprised ten blade passages (nominally).

The design intent blade loading [26] compared to the experimental midspan data at two Reynolds number conditions is shown in Fig. 9. As described in [26], the design calculation was carried out in 2-D on a code assuming fully turbulent flow whereas the midspan of the experiment is influenced by the strong three-dimensionality and secondary flow fields in the low aspect ratio cascade (see Fig. 6) and transitional flow effects. The optimum profile from the design is considered to be aft-loaded and has notably high uncovered turning (19.5°) with respect to the suction-surface curvature.

Table I. Blade Description

Geometry	Value
Axial Chord, C_x	180.57 mm (7.109 inches)
True Chord	194.44 mm (7.655 inches)
Pitch, S	130.00 mm (5.119 inches)
Span, H	152.40 mm (6.000 inches)
Throat Diameter	72.85 mm (2.868 inches)
Leading Edge Diameter	15.16 mm (0.597 inches)
Trailing Edge Diameter	3.30 mm (0.130 inches)
Stagger Angle	20.35°
Inlet Metal Angle	34.20°
Uncovered Turning	19.47°
Exit Metal Angle	−55.54°

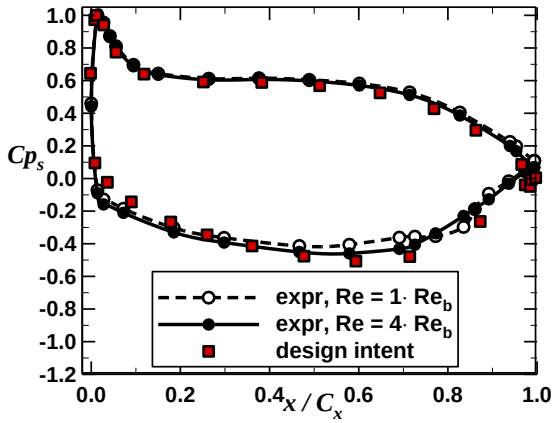

Figure 9. Design Intent and Experimental Data at High and Low Reynolds Numbers and Design Exit Mach Number at i = +5.8°.

Test Configuration

Measurements were acquired for ten incidence angles ranging from −46.0° to +15.8°. Details of the incidence angles and corresponding Zweifel coefficients are listed in Table II. As previously discussed, there are three mission design point angles: takeoff (i= −36.7°), cruise (i = +5.8°), and maximum mission incidence (i = −46.0°). Additional detailed flowfield data and inlet boundary layer measurements were acquired at the cruise and takeoff points.

At each incidence angle setting, data were acquired at the five nominal flow conditions listed in Table III. The design pressure ratio was 1.412 which corresponds to an exit isentropic Mach number of 0.72. A baseline flow condition was established by finding the lowest Reynolds number at which the tunnel could consistently maintain an exit Mach number of 0.72. The baseline Reynolds number, Re_b, was found to be 0.53×10^6. Higher Reynolds number cases were run at 1.06×10^6 and 2.12×10^6. An order-of-magnitude variation in Reynolds number could be achieved by reducing the exit Mach number to 0.35. The lowest Reynolds number point of $2.12 \times 10^5 (0.4 \cdot Re_b)$ could not be achieved at the design exit Mach number due to the limitations of the tunnel operating envelope (see Fig. 2).

Table II. Angles Settings and Zweifel Coefficients

Inlet Angle, β_1	Incidence Angle, i	Zw
50.0°	15.8°	1.22
45.0°	10.8°	1.13
40.0° (Cruise)	5.8°	1.06
34.2°	0.0°	0.99
28.0°	−6.2°	0.92
18.1°	−16.1°	0.82
8.2°	−26.0°	0.74
−2.5° (Takeoff)	−36.7°	0.65
−11.8° (Mission Max-i)	−46.0°	0.58
−16.8°	−51.0°	0.53

Table III. Nominal Flow Conditions

Exit Re_{Cx}	Pressure Ratio	Exit M_{is}	$\delta_{99,1}$ † [in.]	$2\delta_{99,1}/H$ †
2.12×10^6	1.412	0.72	1.16 - 1.23	0.39-0.41
1.06×10^6	1.412	0.72	1.28 - 1.36	0.43-0.45
5.30×10^5	1.412	0.72	1.42 - 1.50	0.47-0.50
5.30×10^5	1.087	0.35	1.40 - 1.49	0.47-0.50
2.12×10^5	1.087	0.35	1.60 - 1.69	0.53-0.56

† Reynolds-scaling estimated range of boundary-layer thickness over ten incidence angle settings.

Boundary Conditions

Inlet Boundary Layer: The estimated inlet boundary-layer thickness range is documented for each flow condition in Table III. The boundary-layer heights were calculated by inlet Reynolds number scaling (turbulent flow) of detailed inlet boundary-layer measurements acquired in Giel et al. [21]. The range in Table III indicates the variation in the boundary-layer thickness for the ten incidence angles and corresponding inlet Reynolds number variations. This Reynolds number scaling was verified during this study by acquiring inlet boundary layer measurements at the take-off and cruise incidence angle for three flow conditions. Figures 10-13 compare the estimated boundary layer

thickness (orange) to the directly calculated thickness from the data (blue) and using two additional scalings. These data confirmed that the use of the Reynolds Number scaling for turbulent flow is adequate for the remainder of the inlet conditions.

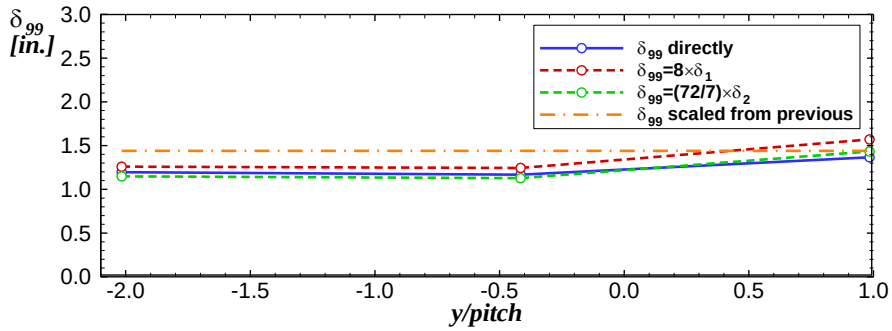

Figure 10. B-L Measurements for i = +5.8°, 1.0·Re_b, $M_{2,i}$ = 0.72.

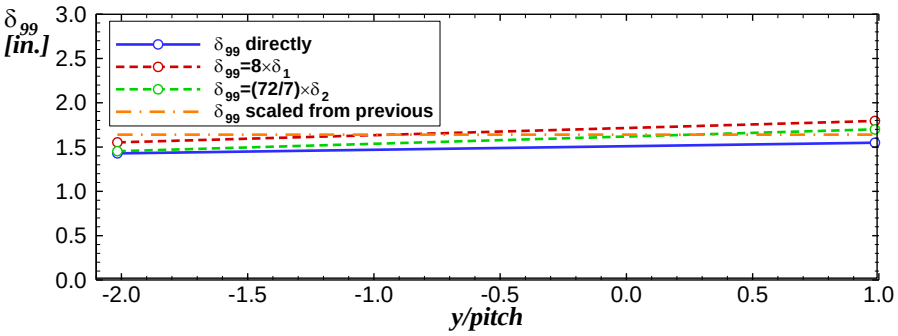

Figure 11. B-L Measurements for i = +5.8°, 0.4·Re_b, $M_{2,i}$ = 0.35.

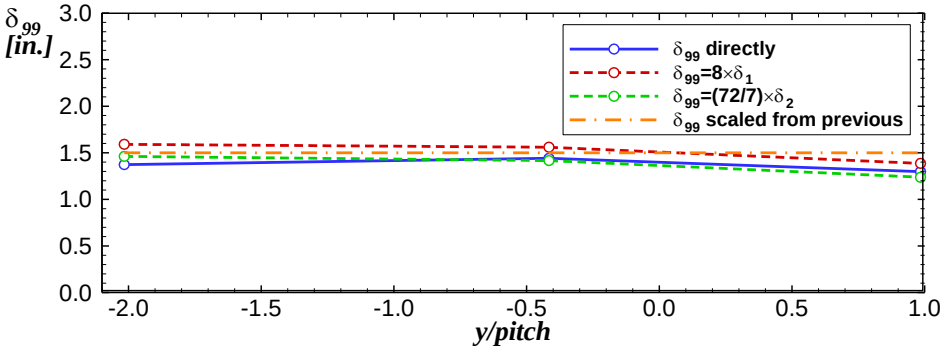

Figure 12. B-L Measurements for i = −36.7°, 1.0·Re_b, $M_{2,i}$ = 0.72.

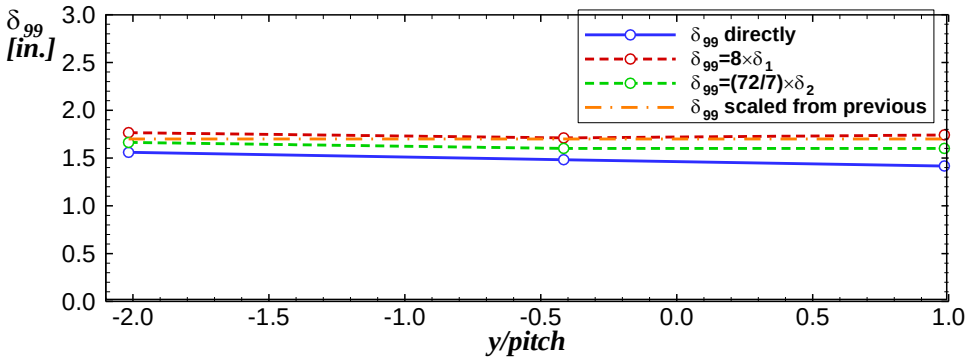

Figure 13. B-L Measurements for $i = -36.7°$, $0.4 \cdot Re_b$, $M_{2,i} = 0.35$.

Inlet Turbulence: The facility has an optional upstream blowing turbulence grid located roughly five axial-chords upstream of the blade row. Hoheisel et al. [16] described the influence of turbulence intensity on the location of 2-D transition and on trailing edge suction-side momentum thickness for the suction surface of front- and aft-loaded blading. The transition point moved upstream with increasing turbulence and appeared always to be associated with a laminar separation bubble. At low turbulence intensities (Tu = 0.8 %), the trailing edge momentum thickness increased with diffusion level. Since the minimum accessible tunnel exit Reynolds number (0.53×10^6) at $M_{2,i}$ = 0.72 of the present effort was significantly higher than that anticipated for engine cruise (e.g., 0.045×10^6 - 0.15×10^6) it was decided to test without the turbulence grid (i.e., at low turbulence) in order to admit transitional flow appropriate to altitude cruise conditions. Outside of this thesis, data have been taken at higher turbulence intensities (Tu = 7% to 8%) to examine the effects of turbulence. As previously mentioned, the inlet turbulence intensity without the grid was documented to range from 0.25% to 0.40%. The integral length scale was found to be 25mm (1.0 inch) to 38mm (1.5 inches) which is largely independent of Reynolds number and immersion in the boundary layer.

Exit Periodicity

The endwall static pressure contours are shown in Fig. 14 for all ten incidence angles. The location of the downstream measurements plane (Station 2) is at roughly x= +5.5 inches and covers the pitch distance $-11.5 \leq y \leq +4.0$. In Fig. 14, the positive incidence angle data show the upper-board and exhaust (near blade 1) creates a low pressure field. At i = +15.8° this difference is almost negligible. Between the blade passages the static pressure appears periodic as will be shown in the downstream survey data. As the incidence is reduced in the negative direction the static pressure non-uniformity increases and influences the downstream pressure field between blades 1-3. This causes the blade-to-blade passage non-uniformity. At i = −46.0° and i = −51.0° the lower flow board induces a negative pressure field affecting blades 9-11.

Focusing on the region of interest (blades 3,4,5) for this test in Fig. 15, the data from the endwall pressure taps located near the Station 2 survey plane (x/C_x = 1.070) are shown for two inlet angles for the baseline Reynolds number and design exit Mach number condition. These data are also compared to the blade base pressures measured on blades 4, 5, and 6. For both incidence angles the static pressure increases in the positive pitch direction. From the contours it can be seen that the pressures are influenced by the downstream exhaust configuration which induces a pitchwise static pressure non-uniformity. The aperiodicity is negligible at positive incidence angles, but increases at the negative incidence angle settings. This aperiodicity will be observable in the flowfield data discussed later.

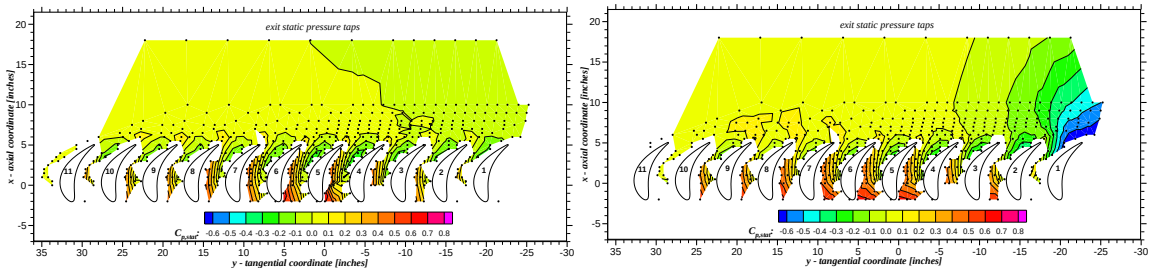

***i* = +15.8°** ***i* = −16.1**

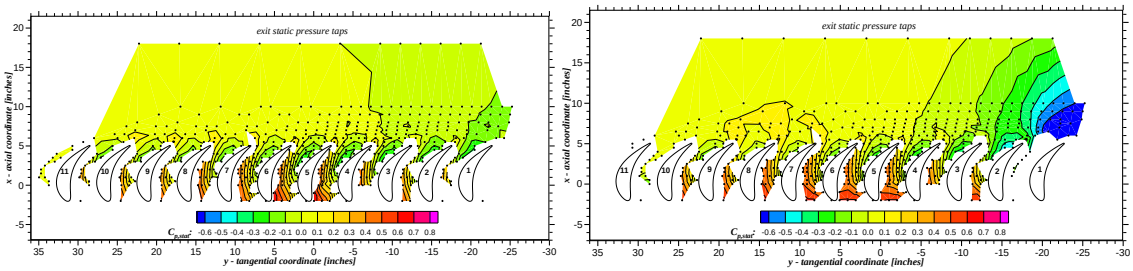

***i* = +10.8°** ***i* = −26.0 °**

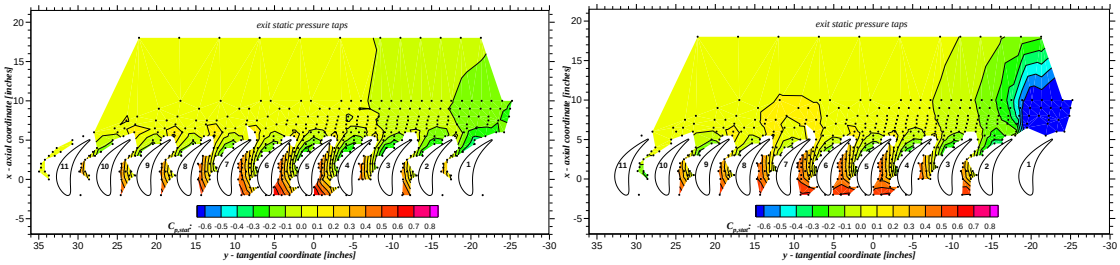

***i* = +5.8°** ***i* = −36.7 °**

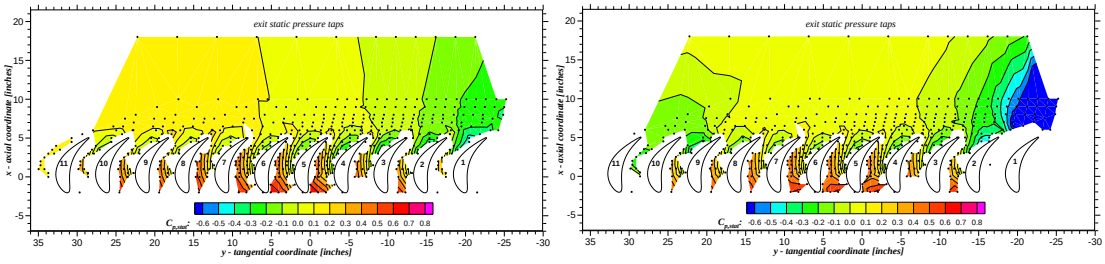

***i* = 0.0°** ***i* = −46.0**

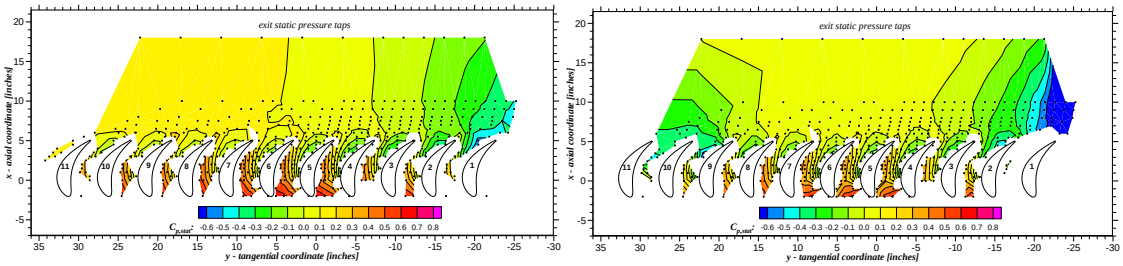

***i* = −6.2 °** ***i* = −51.0 °**

Figure 14. Endwall Static Pressure at $Re_{Cx,2} = 4 \cdot Re_b$, $M_{2,i} = 0.72$.

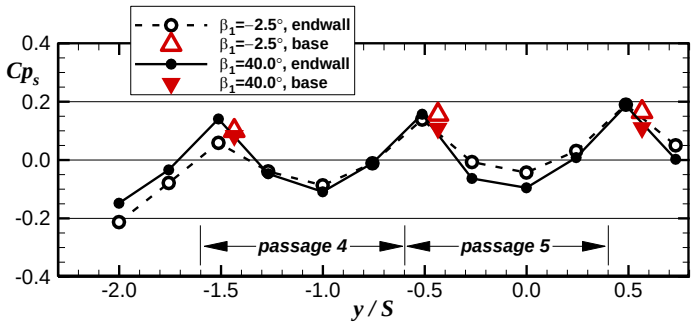

Figure 15. Station 2 Endwall and Midspan Blade Base Pressures at Re_{Cx} = 1.0·Re_b and $M_{2,i}$ = 0.72.

CHAPTER IV

RESULTS

The effects of incidence, Reynolds Number, and Mach number variations on the exit flowfield are explored in this chapter. First, the detailed exit flowfield measurements at the take-off and cruise angles will be discussed which will give a good initial comparison of the flowfield for negative and positive incidence conditions. The impact of incidence change on secondary flowfield effects and blade loading will be very noticeable. This will be supported by the blade loading data for the ten incidence angles. Once the flowfield and blade loading trends are established, the midspan total-pressures and exit flow angles will be discussed.

3-D Flowfield Results

Survey Data

Detailed exit flowfield measurements were obtained for the cruise (i = +5.8°) and takeoff (i = −36.7°) incidence angles at the baseline Reynolds number (Re_b = 530,000) and design exit Mach number ($M_{2,i}$ = 0.72). To look at the effects of Reynolds number

and Mach number, detailed measurements were also obtained at a low flow condition ($Re_{Cx,2}$ = 212,000 and $M_{2,i}$ = 0.35) and the takeoff incidence setting. Data were taken at 26 spanwise locations over 62 pitchwise points.

The total-pressure contours in Fig. 16 show that at the positive incidence angle (Fig. 16a) the blade is highly loaded, producing strong secondary flows which drive the endwall flow to and along the suction side of the blade. The blade loading is reduced and the flow becomes very two-dimensional at the negative incidence angle (Fig 16b). The contours of total-pressure coefficient remain largely unchanged as the Reynolds number and Mach number are reduced as shown in Fig. 16c.

A detailed single-passage view of the secondary flow vectors and pitch and yaw angles are shown for the baseline flow conditions at the positive (Fig. 17) and negative (Fig. 18) incidence angles. The impact of secondary flows is evident for i = +5.8°. The flow vectors and pitch angles show strong overturning near the hub (z = 0). At y/S = −0.45 and z/H = 0.33 in Fig. 17a the flow vectors show the core of the horseshoe vortex. This is also evident in the pitch and yaw angle data. For i = −36.7°, the secondary flow vectors, and the pitch and yaw angle show little variation due to the two-dimensionality of the flowfield.

The total pressure data of the three- and five-hole probe measurements were in good agreement for both incidence angles as seen at z/H = 0.042. Figure 16 also shows reasonable periodicity between passages 4 and 5. Consistent with the downstream endwall static pressure contours in Fig. 14, there is a slight aperiodicity observed in Passage 6.

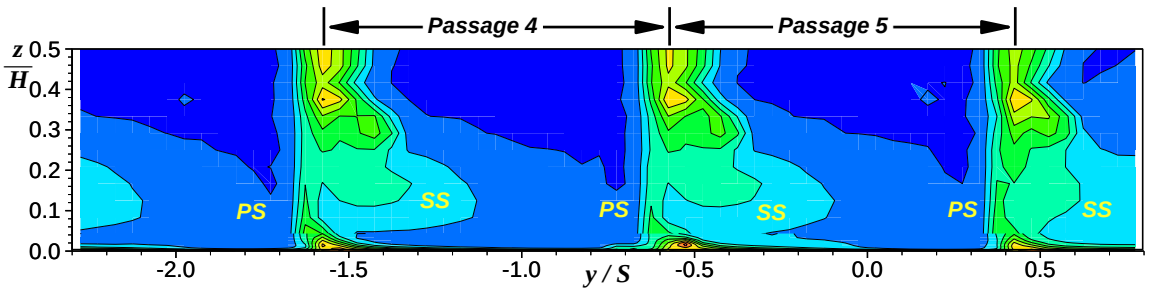

a) i = +5.8°, $M_{2,i}$ = 0.72, $Re_{Cx,2}$ = Re_b.

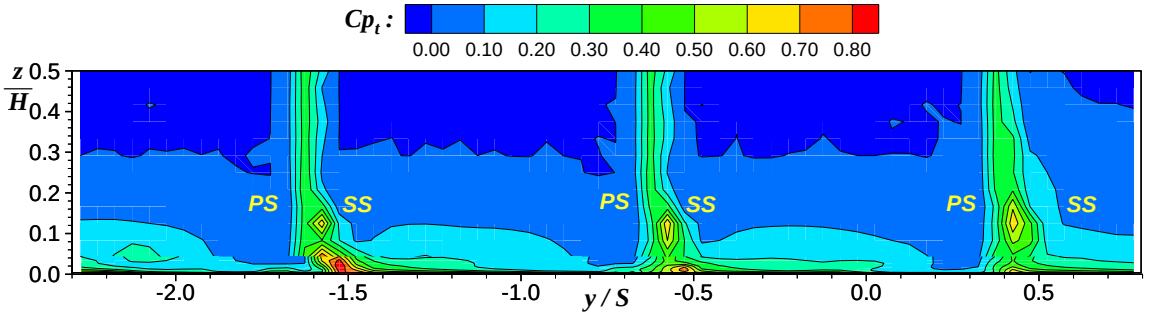

b) i = −36.7°, $M_{2,i}$ = 0.67, $Re_{Cx,2}$ = Re_b.

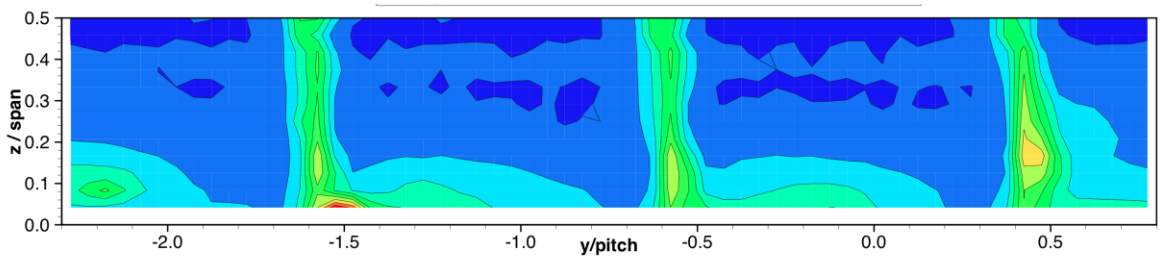

b) i = −36.7°, $M_{2,i}$ = 0.35, $Re_{Cx,2}$ = 0.4·Re_b.

Figure 16. Total Pressure Coefficient Contours Over Three Passages.

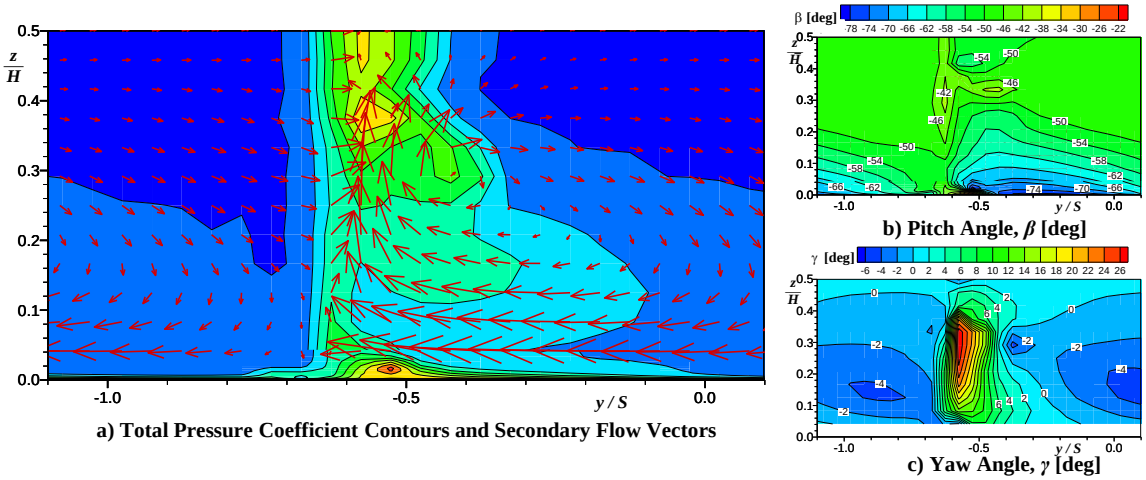

Figure 17. Detailed View of Flow at i = +5.8°, $Re_{Cx,2}$ = 5.30×10^5 (Re_b), $M_{2,i}$ = 0.72.

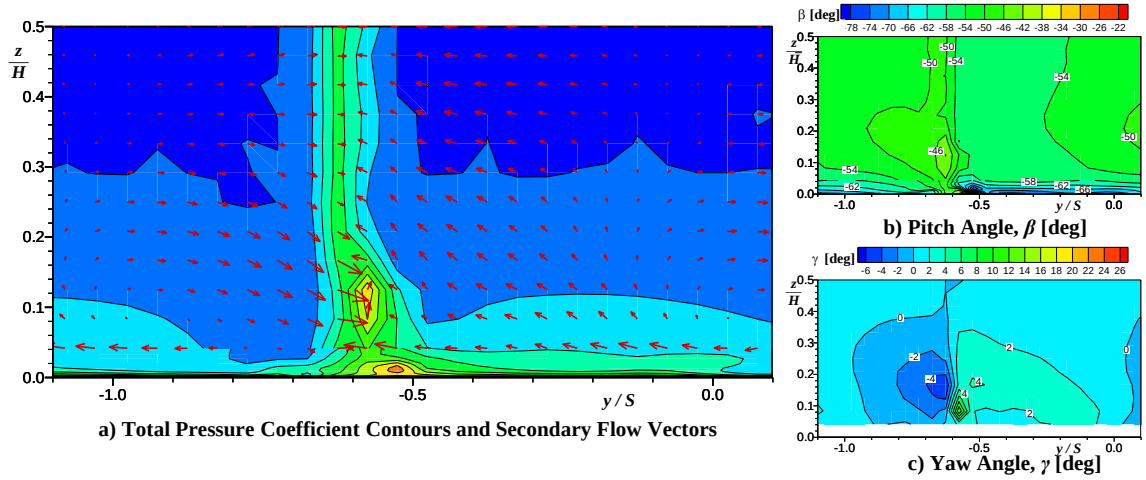

Figure 18. Detailed View of Flow at i = −36.7°, $Re_{Cx,2}$ = 5.30×10^5 (Re_b), $M_{2,i}$ = 0.67.

Pitchwise integrations of the total-pressure coefficient, pitch angle, and yaw angle were calculated at each spanwise immersion for i = +5.8° (Fig. 19) and i = −36.7° (Fig. 20 and Fig. 21). Area-averaging of the total pressure was performed so that calculated loss coefficients would account for loss production both within the blade passage and in downstream mixing. The area-averaged total-pressure coefficient (Fig. 19a and 19b)

reflects strong spanwise variation in the secondary-flow field; the thick inlet boundary-layer fluid is thinned out near the hub and transported to a higher span section on the blade suction side. The estimated inlet boundary layer, noted in Table III, for this flow condition is 1.44 inches, which accounts for roughly 24% of the blade span. As seen in the flowfield contours (Figs. 17), the horseshoe vortex and its core location can be seen in Fig. 19c and 19d at z/H = 0.33. The pitch angle in Fig. 19c show the flow is always overturned near the hub. The point of minimum turning is located at z/H = 0.33. This is the same spanwise location of the maximum yaw angle shown in Fig. 19d.

The integrations at $i = -36.7°$ are shown in Fig. 20 at the baseline flow conditions. The inlet boundary-layer thickness was 1.50 inches, roughly 50% of the half-span; due to the two-dimensionality of the flow at this incidence angle, the boundary-layer thickness at the exit remains nearly consistent through the blades. The pitch angle in Fig. 20c reflects overturning at the endwall; further up the span, the flow tends towards the exit metal angle and remains constant spanwise. The integrations at the same incidence angle but at a reduced Reynolds and Mach number are shown in Figure 21. The trends are the same for both flow conditions. Only five-hole probe data were obtained due to tunnel test-time constraints.

The total-pressure integrations for both angles show good agreement between each passage and between the three-hole and five-hole probes. The yaw angle data could only be acquired with the five-hole probe. Passage-to-passage differences in yaw angles and the average offset from 0° are within the measurement uncertainty.

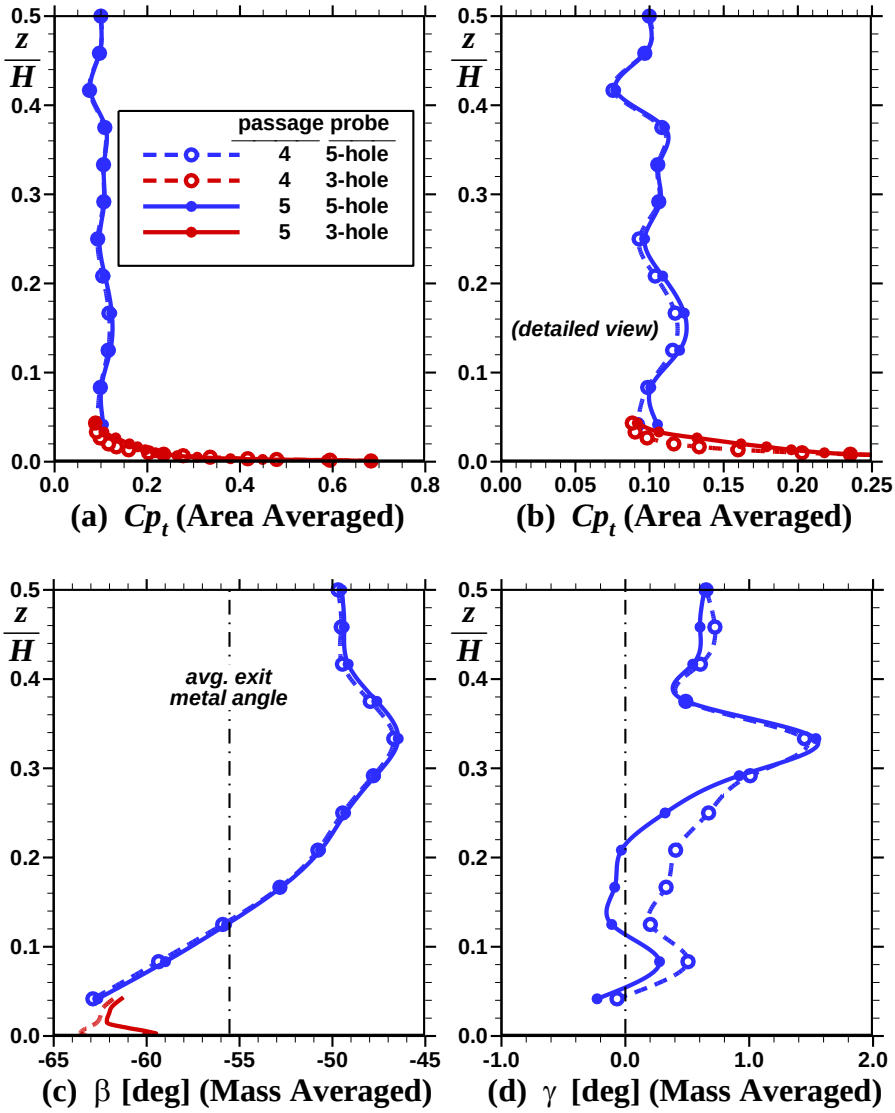

Figure 19. Pitchwise Integrations for i = +5.8° at Re_b and $M_{2,i}$ = 0.72.

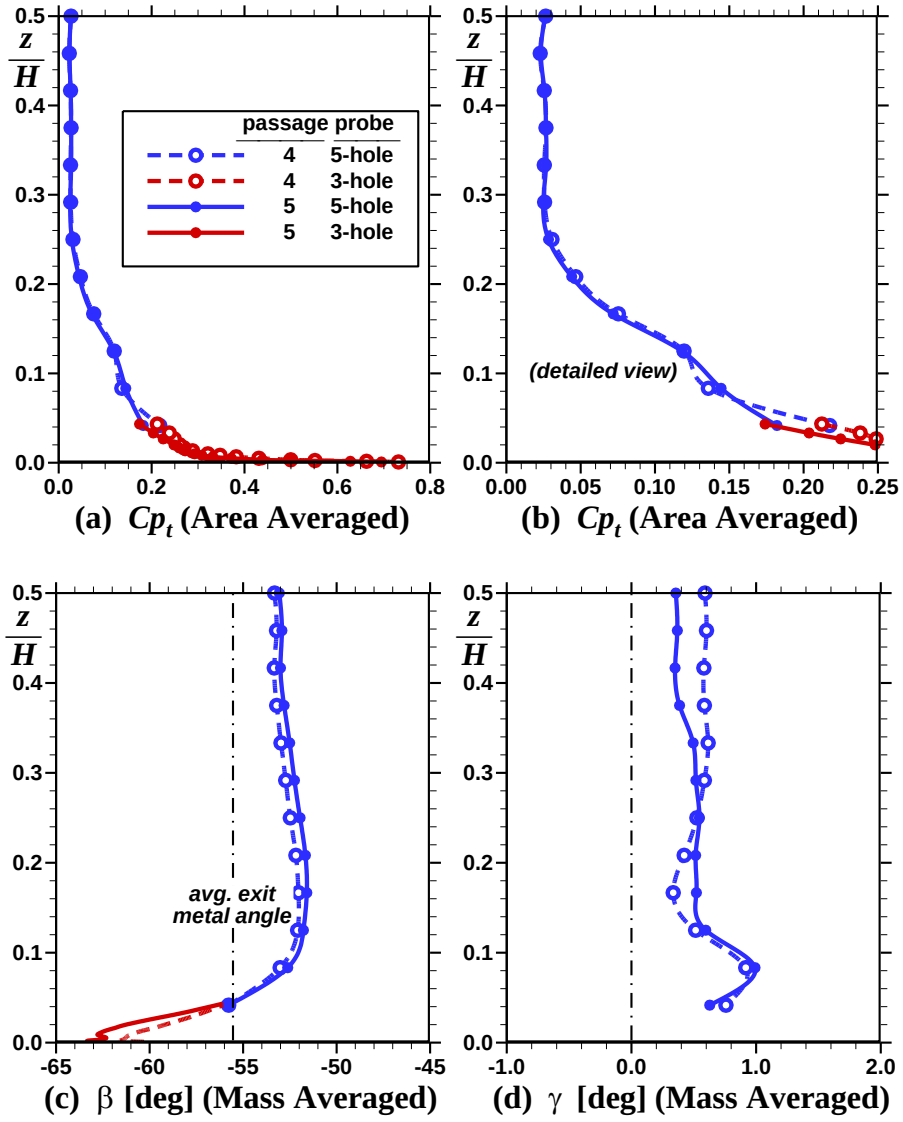

Figure 20. Pitchwise Integrations for i = −36.7° at Re_b and $M_{2,i}$ = 0.72.

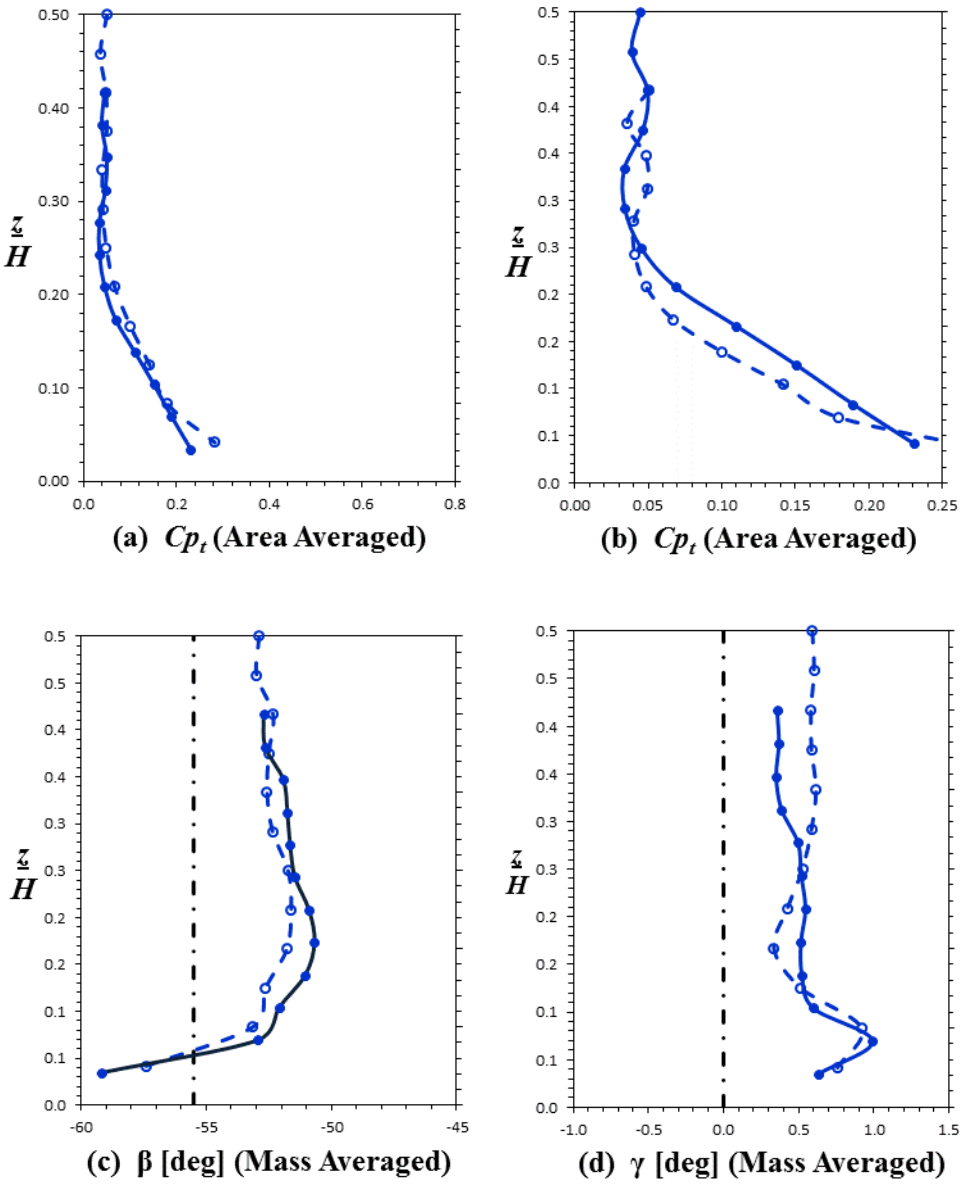

Figure 21. Pitchwise Integrations for i = −36.7° at 0.4·Re_b and $M_{2,i}$ = 0.35.

Table IV. Passage Average Integrations

i	Passage	Exit M_{is}	$Re_{Cx,2}$	ω
+5.8°	4	0.72	530,000	0.00044
+5.8°	5	0.72	530,000	0.00287
−36.7°	4	0.72	530,000	0.02319
−36.7°	5	0.72	530,000	0.02109
−36.7°	4	0.35	212,000	0.02481
−36.7°	5	0.35	212,000	0.02610

Blade Loading

The effects of incidence and Reynolds number on blade loading are shown in Fig. 22 for five selected incidence cases. The nominal flow conditions are listed above the plots. The loading plots are arranged with the highest Reynolds number ($4 \cdot Re_b$) on the left column decreasing to the minimum tested Reynolds number on the right most column ($0.4 \cdot Re_b$). The incidence angle begins with the highest positive incidence in the top row and decreases to the lowest negative incidence at the bottom row.

There are several notable observations from these data. The blade loading data for i = +15.8° confirms the three-dimensional characteristics observed in the total-pressure contours for the positive incidence in Figure 16. The three dimensionality of the flow can be observed by the spanwise variation in the static pressures represented by the colored symbols. A majority of the blade surface had mid-span static taps which are shown as the black symbols. This extreme positive incidence is clearly noted to have the highest loading of the other incidence angles, which increases with decreasing Reynolds and Mach number. For all five flow conditions, the suction surface exhibits a neutral pressure gradient region, followed by an abrupt diffusion near x/C_x = 0.45. This jump is indicative of a reattachment following a laminar separation bubble (see Hoheisel et al. [14]). For this incidence and all subsequent incidence angles, the data show excellent blade-to-blade periodicity.

As incidence decreases, the front portions of the blades unload and the secondary flow effects diminish. At zero incidence the blade still exhibits a suction side separation that has moved farther aft on the blade at x/C_x = 0.8. This separation becomes more prominent at the lowest flow condition. With decreasing incidence, negative loading is

measured at the front portions of the blade. At $i = -16.1°$, a suction side separation is again observed at the lowest flow condition. When the incidence decreases to $i = -36.7°$, a pressure-side separation is observed at the lowest flow condition and is reflected in the midspan exit surveys shown later. At the extreme negative incidence of $i = -51.0°$ the pressure side is separated for all Reynolds and Mach numbers. This is consistent with Yamamoto and Nouse [12] and Brear et al. [25]. A suction surface separation/reattachment is still observed which occurs near $x/C_x = 0.59$.

The effects of exit Mach number on blade loading are shown in Fig. 23. All data in this figure were acquired at the baseline Reynolds number. The loading increases and the location of minimum Cp_s moves forward with decreasing $M_{2,i}$. The increased diffusion causes the suction-surface reattachment points to move forward.

The net blade loading was calculated for the five incidence angles and plotted in Figure 24. It is clearly shown that as the incidence decreases to a large negative values, the overall loading decreases. The loading levels are higher for the reduced Mach number conditions at incidence angles between $+15.8° \geq i \geq -16.1°$. The net loading converges at $-36.7°$ for all Mach number conditions. At negative incidence angles larger than $-36.7°$ the net loading is lower for the low Mach number conditions. How this relates to losses will be discussed in the following chapter.

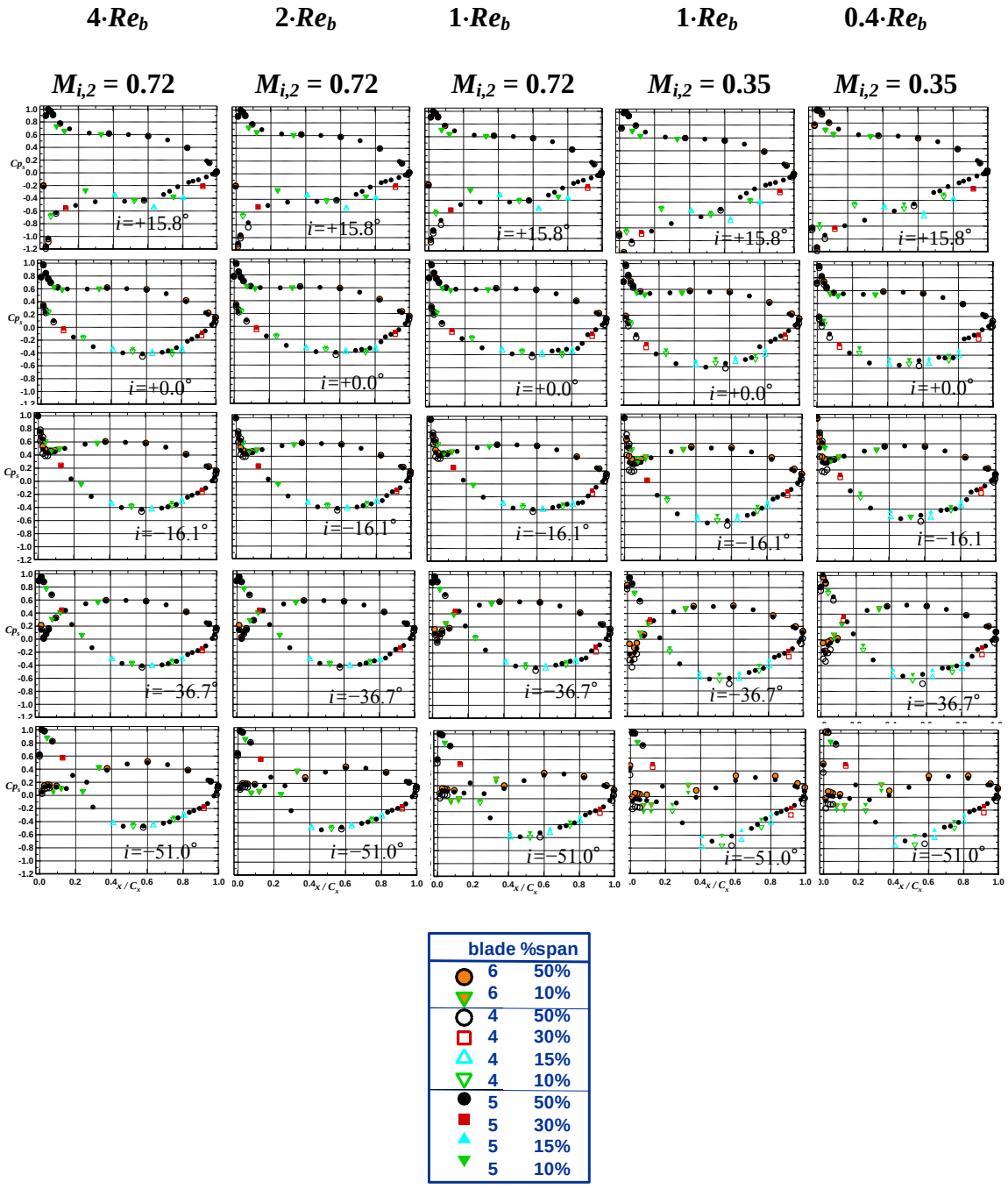

Figure 22. Blade Loading (Cp_s vs. x/C_x) for five incidence angles at five flow conditions.

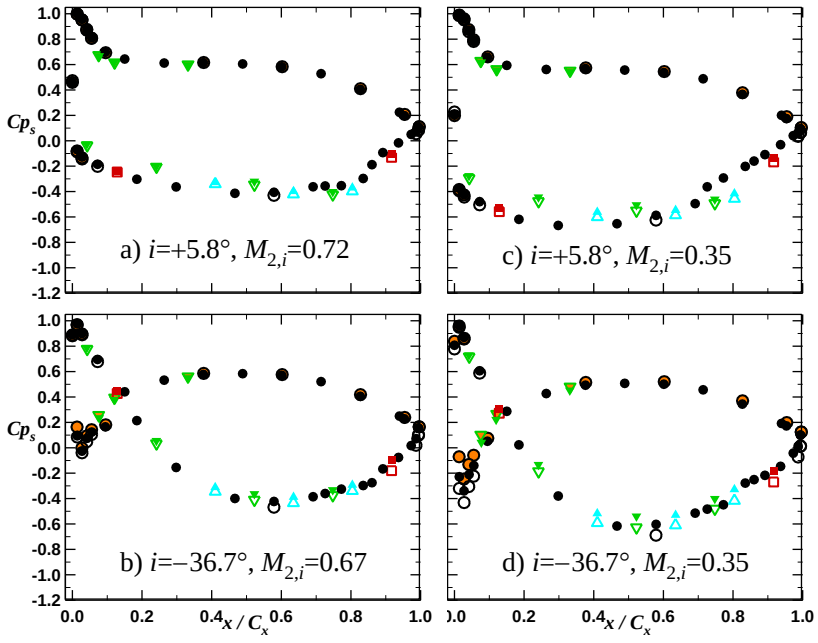

Figure 23. Blade Loading – Effects of Exit Mach Number at $Re_{Cx,2}$= 5.30×10^5 (Re_b).

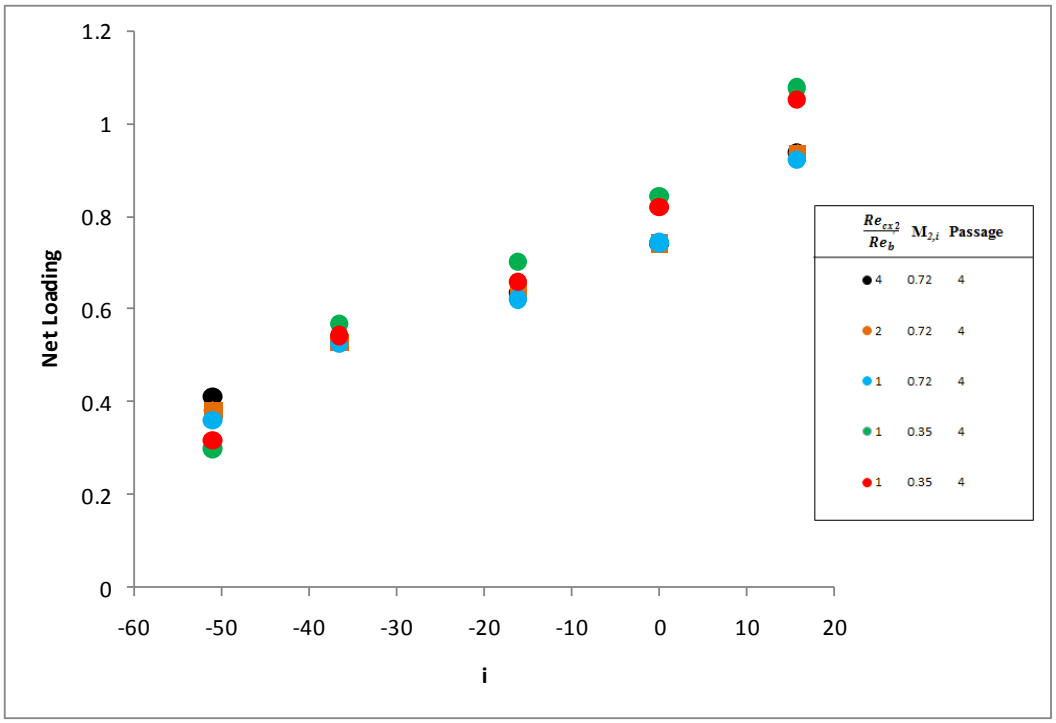

Figure 24. Net Loading vs. Incidence

2-D Midspan Results

Exit Survey Data

Midspan total-pressure and exit flow angle (pitch angle) surveys were measured for all ten incidence angles at five flow conditions. Figures 25 to 29 show the effects of Reynolds number and Mach number variations for a sample of five incidence angles. At the positive incidence angle in Fig. 25, the influence of the high blade loading and secondary flows on the mid-span total-pressure wake profile is observed. As the Reynolds Number is reduced, the suction-side wake width increases. This is due to the suction-side separation observed in the blade loading. At the baseline Reynolds number, $1.0 \cdot Re_b$, the wake width remains constant as the exit Mach number is varied from 0.72 (design) to 0.35. The Mach number influences the exit angle as seen in the bottom plot shown in Figure 25 but the exit flow angle is relatively independent of Reynolds number. As the Reynolds and Mach numbers decrease, the exit flow angle decreases and stays at or above the pressure-side exit metal angle.

As the incidence decreases, it is noted that the blade becomes unloaded and the flow becomes more two-dimensional. The influence of the suction side separation decreases, which results in a narrower wake profile as incidence decreases (Fig. 26-28). For these incidence angles, the trends are still the same; as the Reynolds number decreases, the wake width and depth increases. The exit angles begin to increase in the negative direction and generally remain between the pressure surface exit metal angle and the average exit metal angle.

At an incidence of −36.7° (Fig. 28), there is little variation in the wake profile due to changes in the Reynolds and Mach number. The overall levels of Cp_t have decreased

at this incidence. At the lowest Reynolds number ($0.4 \cdot Re_b$) there is a small wake width increase on the pressure side. This becomes greatly exacerbated at the largest negative incidence tested ($i = -51.0°$, Fig. 29) where the pressure-side separation is evident. This separation covers most of the blade passage and its influence increases with decreasing Reynolds number. There is also a small variation on the suction side as well with decreasing Reynolds number. At this angle, it is also noted that the wake profile remains unchanged at the fixed Mach number ($M_{2,i} = 0.35$) condition as Reynolds number is varied from $1.0 \cdot Re_b$ to $0.4 \cdot Re_b$. The exit flow angle varies little with Reynolds number and remains near the average exit metal angle, except for the highest Reynolds number ($4.0 \cdot Re_b$) where the exit metal angle is lower and is consistent with the exit angles measured in Figure 28. The exit angles and loss profiles indicate that at the extreme negative incidence conditions, as Reynolds number is decreased, the pressure side separation-induced wake thickens substantially. The increased aerodynamic blockage on the pressure-side resets the aerodynamic throat upstream and effects increased turning and a more negative discharge angle.

The effects of incidence-angle variation at the highest and lowest Mach number conditions are summarized in Figs. 30 and 31, respectively. An order of magnitude variation in Reynolds number is reflected between these two figures. The three incidence angles shown represent the cruise ($i = +5.8°$), takeoff ($i = -36.7°$), and maximum mission incidence ($i = -46.0°$) angles. At the highest Reynolds number ($4.0 \cdot Re_b$) in Fig. 30, the positive incidence produces an overall higher loss and decreases with decreasing incidence and loading. In Fig. 31, at the lowest Reynolds number ($0.4 \cdot Re_b$) and Mach number of 0.35, large incidence variations are observed. The positive incidence shows a

large suction side wake which is consistent with the suction-side separation observed in the blade loading. As the incidence decreases, the blade is unloaded and the losses decrease. At the takeoff incidence the suction-side is attached and a slight increase in pressure-side losses is observed. As the negative incidence increases further, an extensive pressure-side separation is evident.

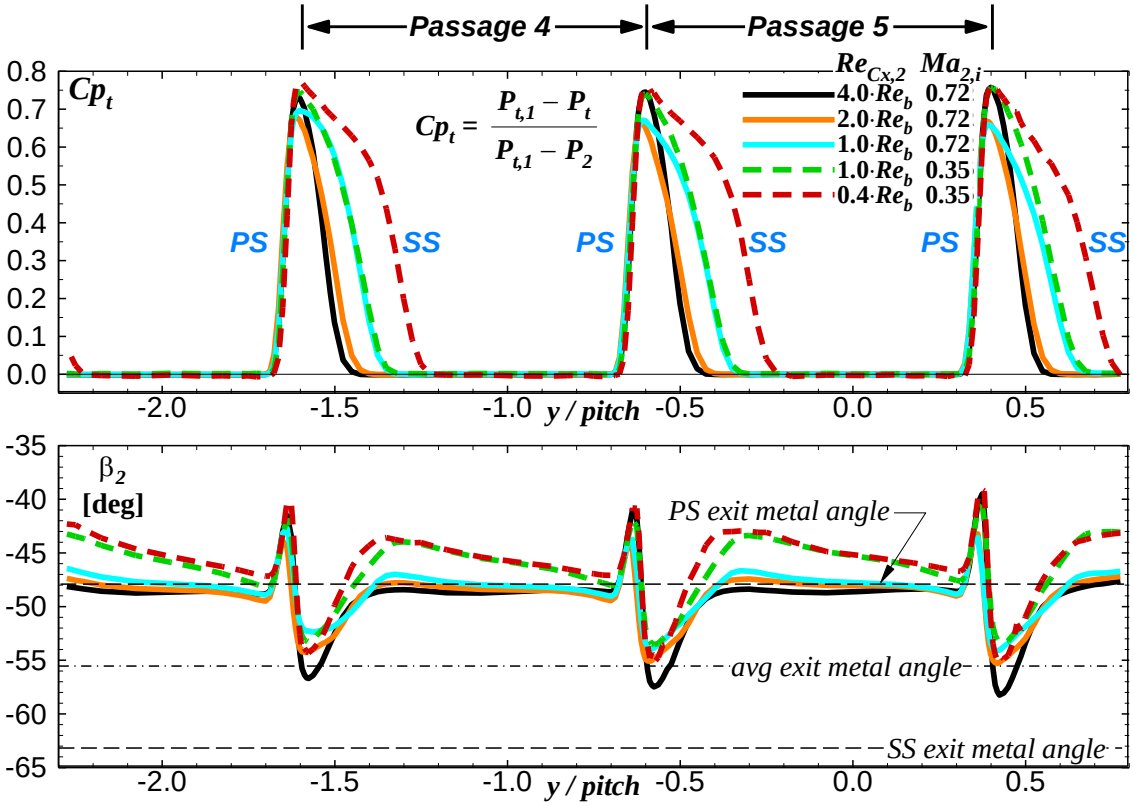

Figure 25. Effects of Reynolds Number and Exit Mach Number at *i* = +10.8°.

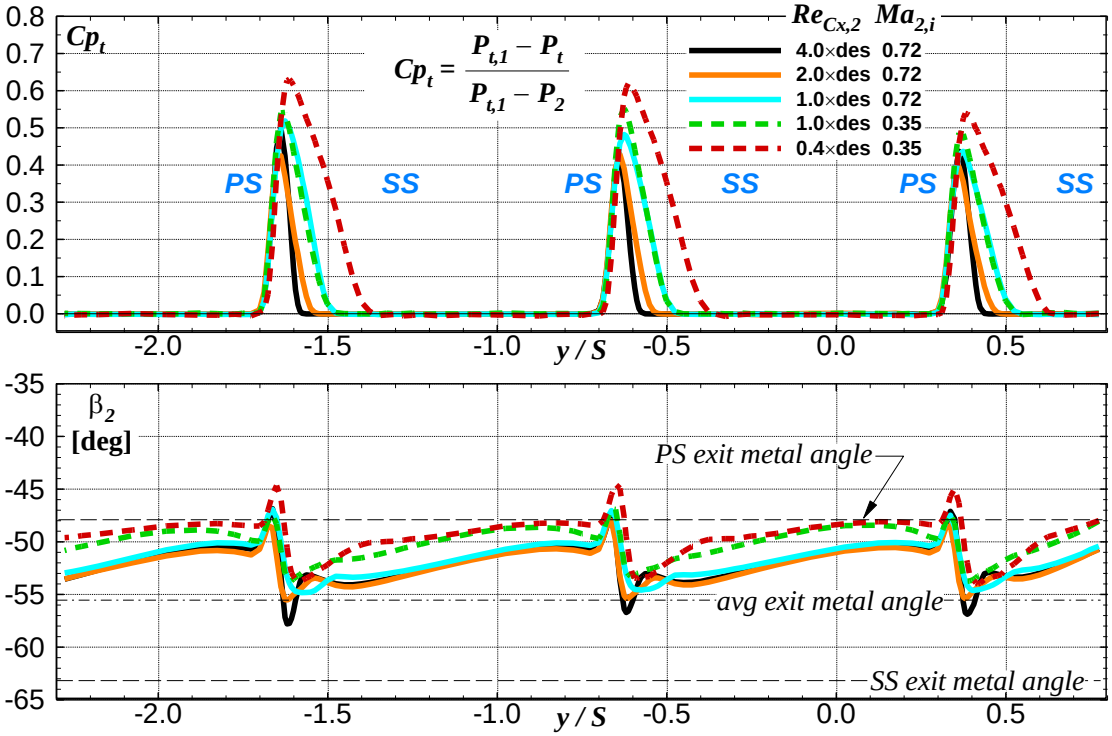

Figure 26. Effects of Reynolds Number and Exit Mach Number at i = 0.0°.

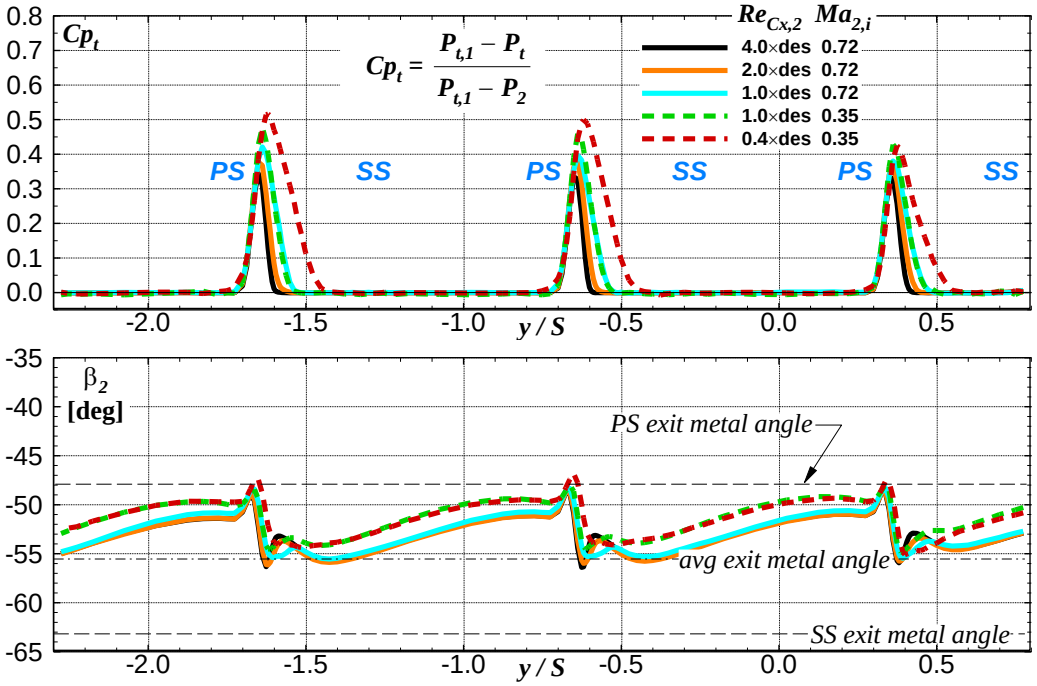

Figure 27. Effects of Reynolds Number and Exit Mach Number at $i = -16.1°$.

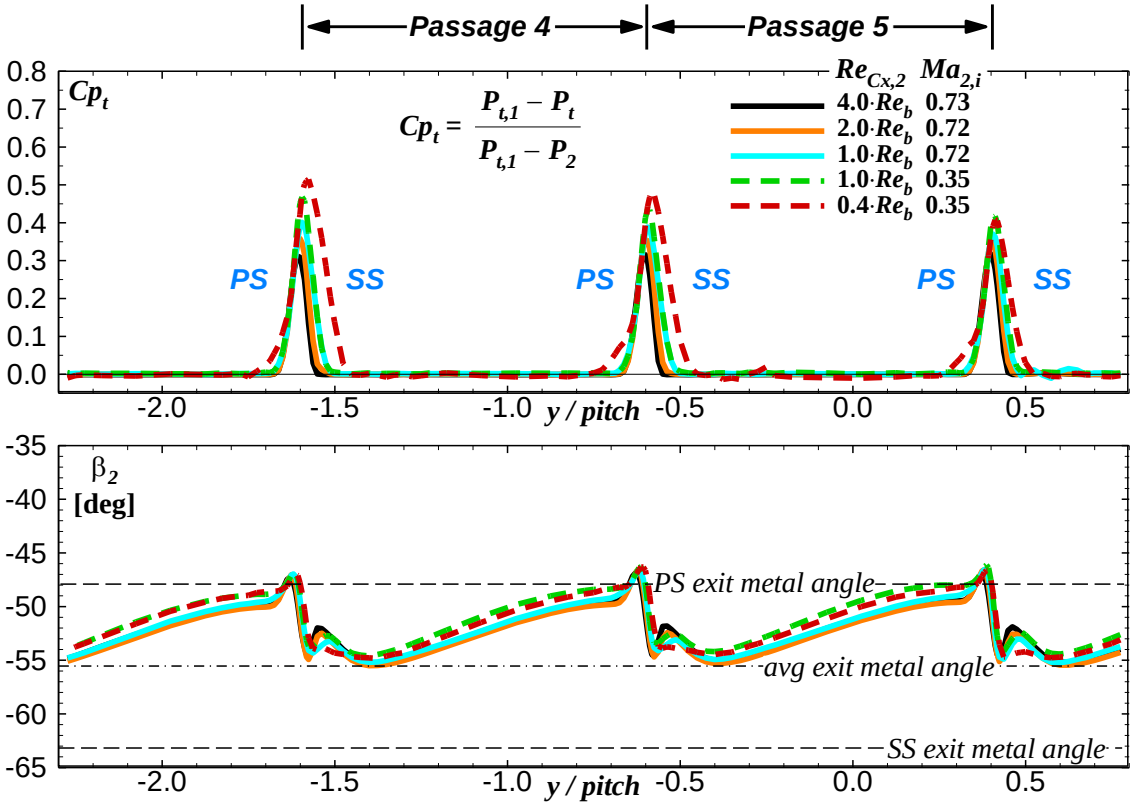

Figure 28. Effects of Reynolds Number and Exit Mach Number at $i = -36.7°$.

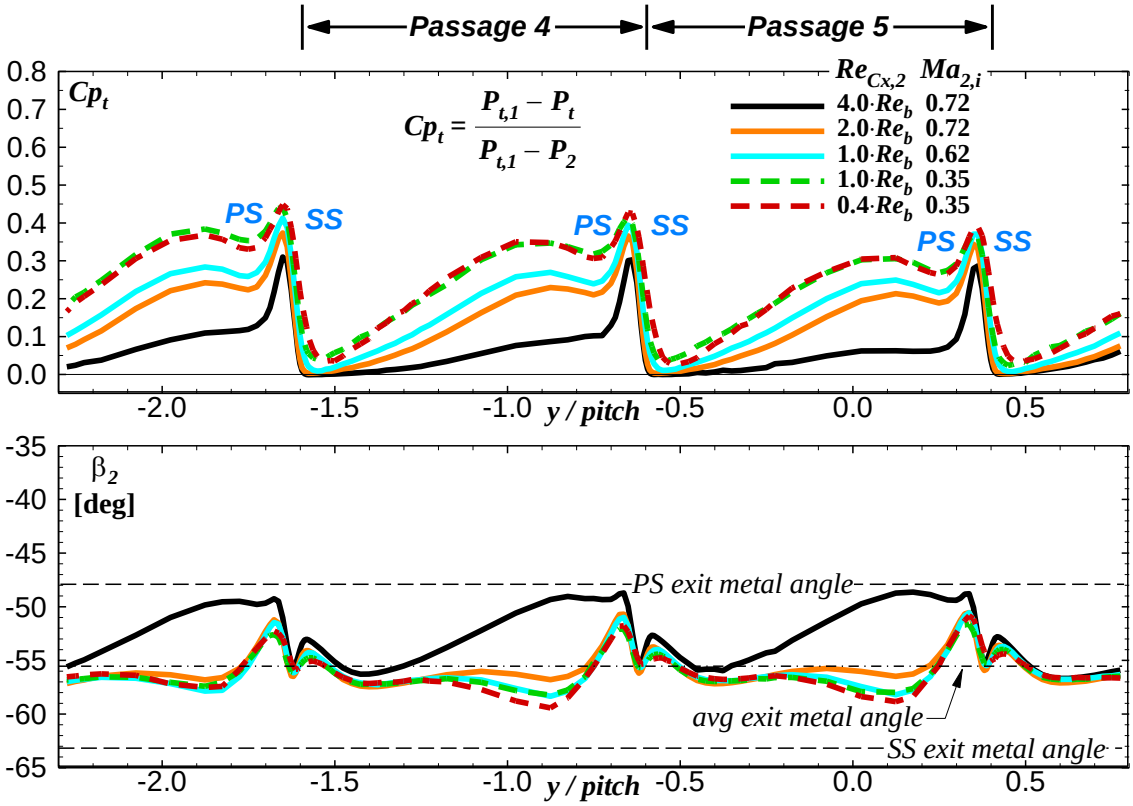

Figure 29. Effects of Reynolds Number and Exit Mach Number at $i = -51.0°$.

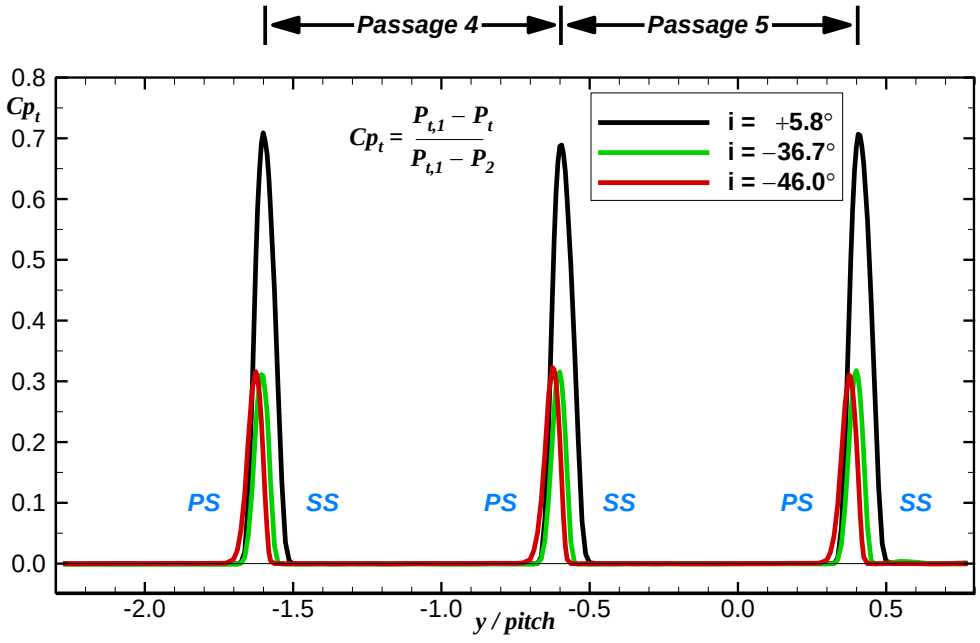

Figure 30. Effects of incidence angle at $Re_{Cx,2} = 2.12\times10^6$ ($4\cdot Re_b$) and $M_{2,i} = 0.72$.

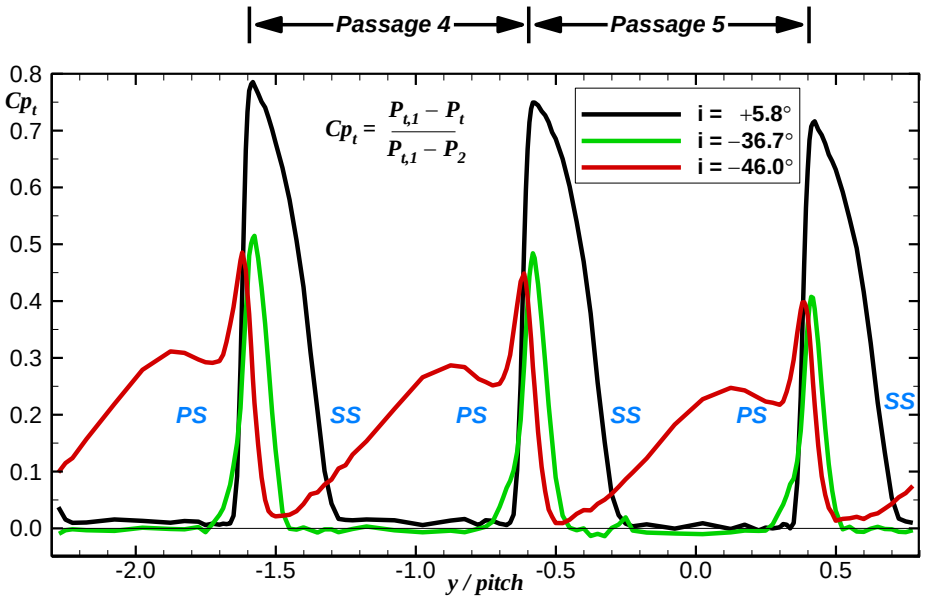

Figure 31. Effects of incidence angle at $Re_{Cx,2} = 2.12\times10^5$ ($0.4\cdot Re_b$) and $M_{2,i} = 0.35$.

Midspan Loss Coefficients

Area-averaged integrations of the total-pressure data were used to calculate midspan profile loss coefficients, ω, for each incidence angle and flow condition. Midspan loss coefficients are plotted as a function of incidence in Fig. 32. The integrations were calculated separately over two complete passages, 4 and 5. Passage-to-passage variations are noted at the extreme negative incidence angles. As expected, as the Reynolds number decreases, loss levels increase and the loss bucket narrows. For the two conditions where the baseline Reynolds number (Re_b) is held constant and the Mach number is varied from $M_{2,i} = 0.72$ to $M_{2,i} = 0.35$, the loss levels are independent of Mach number except at the extreme positive (i = +15.8°) and negative (i = −46.0°, and −51.0°) incidence angles.

The midspan profile loss coefficients were plotted as a function of Reynolds number. The power-law functionality was examined and found to be indicative of regions of transitional flow, with the higher Reynolds numbers scaling with a −0.1 to −0.2 exponent (turbulent) and the lower Reynolds number scaling with −0.5 exponent (laminar); however, the power-law exponent was found to vary with incidence angle. Nonetheless, it is interesting that the strongest collapse of the overall bucket on Reynolds number, shown in Fig. 33, was obtained with a $\omega \propto Re^{-0.5}$ scaling, indicative of a significant influence of laminar flow on the midspan loss levels.

The same loss coefficient data (Fig. 32) were plotted in terms of reduced loss and incidence according to the Ainley-Mathieson (A-M) scaling (ω/ω_i vs. i/i_s) [27], shown in Fig. 34. For each loss curve, $\omega_s = 2\times\omega_{i=0}$ and the stalling incidence, i_s, is the incidence corresponding to ω_s. The A-M scaling strongly collapses the data down to $i/i_s = -5°$. Thus a canonical shape can be used to represent the data, with the following caveat: the narrowing of the loss bucket is found to be a function of Reynolds number to an extent beyond that tared out by the scaling on the stalling incidence. That is, the lack of collapse at the extreme negative incidence range, though consistent in Reynolds number, reflects a rate of change that is not tared out by a change in stalling incidence with Reynolds number.

To account for blade loading, the midspan losses were plotted as a function of the net blade loading as shown in Figure 35. Overall, the losses increase with decreasing Reynolds number as expected. There is a region of net loading (0.53 – 0.74) where there is little variation in loss level and the loss is at the minimum. From the loading data in Fig. 22 it is noted in this region that the flow over the blade becomes two-dimensional

and a loss-generating suction surface separation occurs at the lower flow conditions. There are high losses at the minimum net blade loading which is due to the gross separation on the blade pressure surface. As the net loading increases, secondary flows begin to develop, as seen in the flow field data, and a suction side separation causes the loss levels to increase.

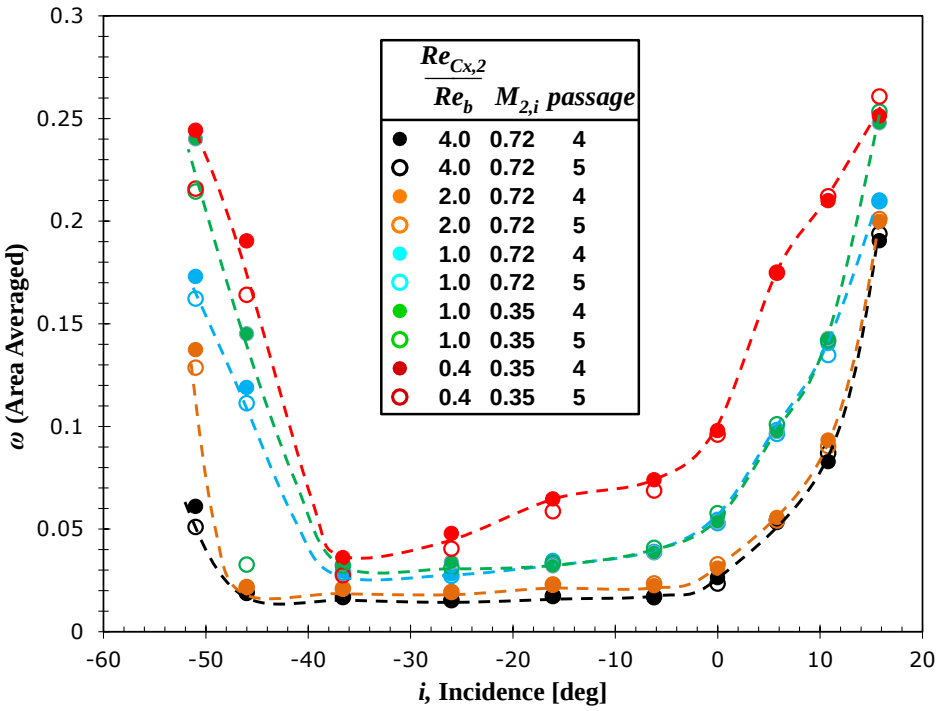

Figure 32. Midspan Loss vs. Incidence.

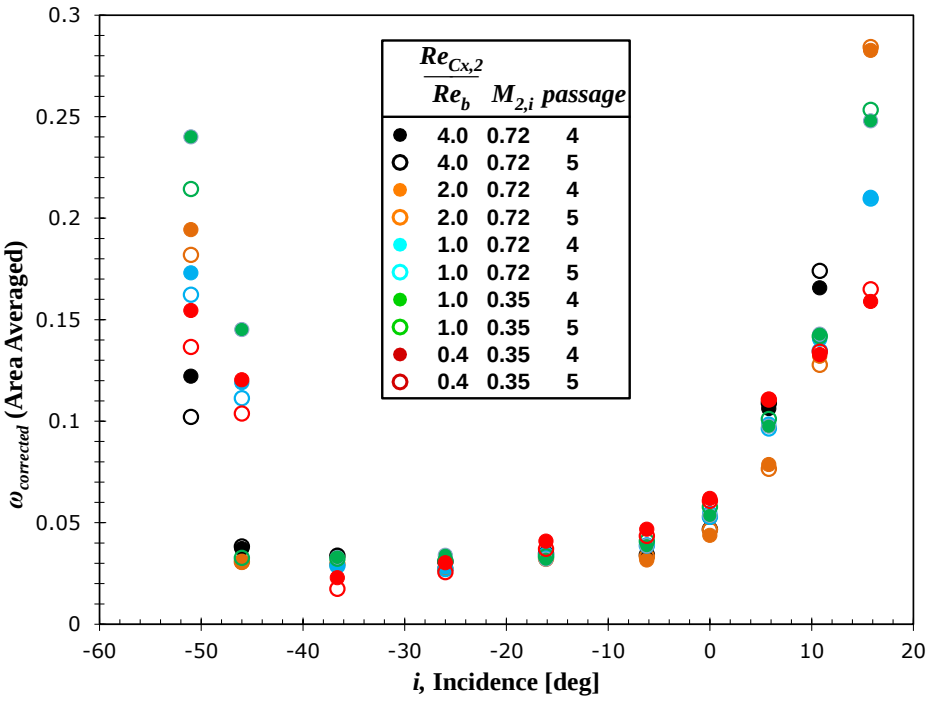

Figure 33. $Re^{-0.5}$ Scaled Midspan Loss vs. Incidence.

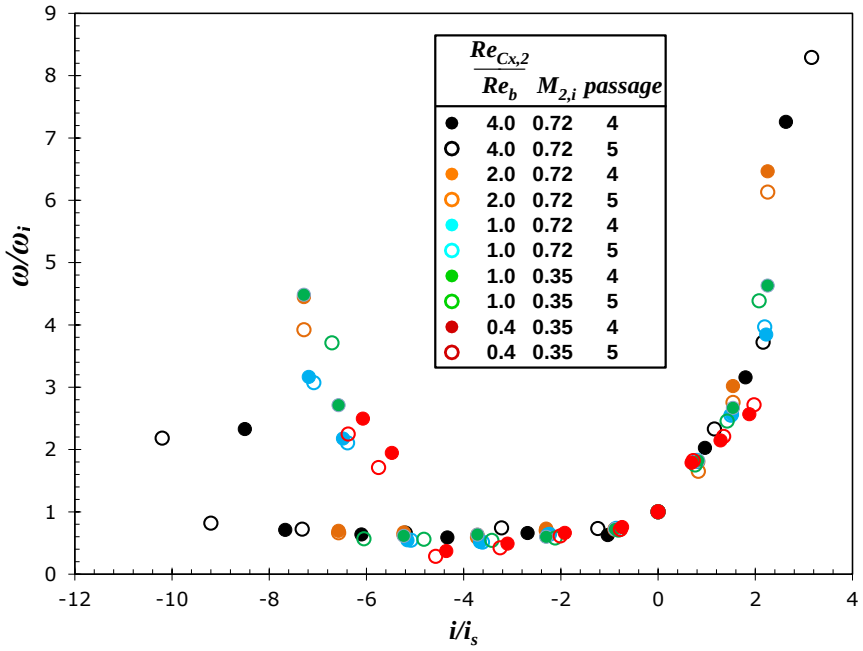

Figure 34. Midspan Loss Bucket on Ainley-Mathieson Scaling.

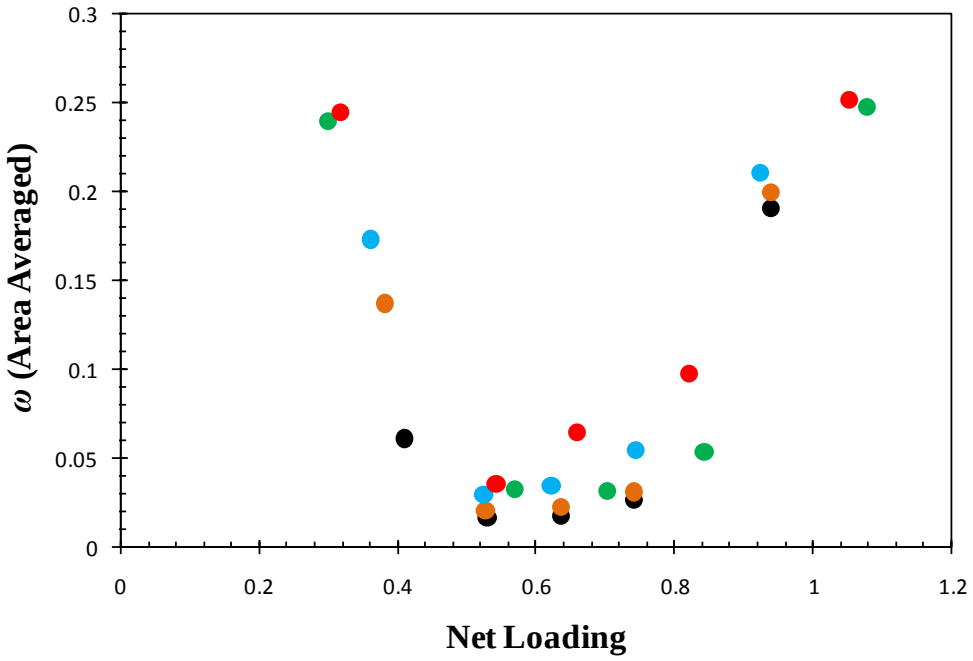

Figure 35. Midspan Loss vs. Net blade Loading.

Midspan Turning

The deviation angle, or the difference between the exit flow angle and the mean exit metal angle ($\Delta\beta_2 = \beta_2 + 55.54°$), is plotted as a function of incidence in Fig. 36. Deviation angles asymptotically (see $i \geq -26.0°$) approach $\Delta\beta_2 = 2°$ as the blade unloads at the design Mach numbers ($M_{2,i}$= 0.72) and $\Delta\beta_2 = 4°$ at the lower $M_{2,i}$= 0.35 conditions. Deviation angles at cruise, i = +5.8°, are between $\Delta\beta_2 = 5°$ ($M_{2,i}$ = 0.72) and $\Delta\beta_2 = 9°$ ($M_{2,i}$= 0.35). At the lower Reynolds number and extreme negative incidence angles, the exit flow angles shifts to the exit metal angle. The increased aerodynamic blockage on the pressure side of the airfoil at reduced Reynolds numbers is thought to affect the more negative discharge angle.

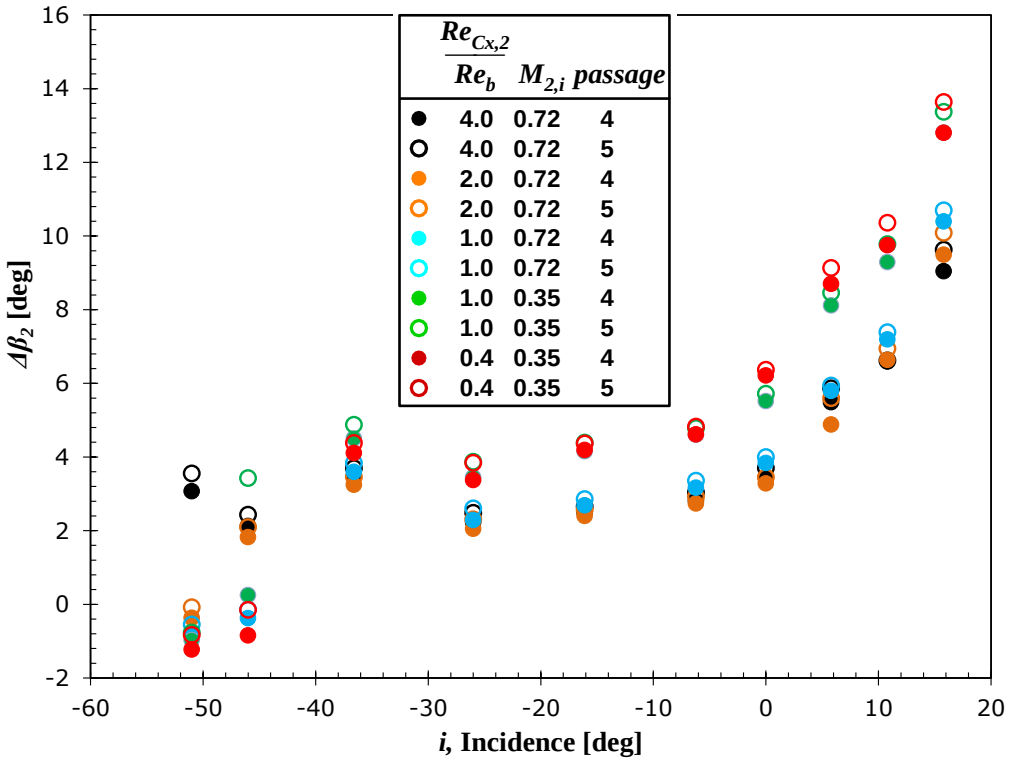

Figure. 36 Midspan Deviation Angle From Exit Metal Angle as Function of Incidence and Reynolds Number.

CHAPTER V

CONCLUSIONS

This thesis was intended to advance the understanding of aerodynamic effect of large incidence angle and Reynolds number variations by documenting and explaining measurements on a variable-speed power-turbine blade. This work expands on previous work in the open literature by documenting inlet and exit characteristics, exit total pressure, flow angles, and blade loading at relevant Reynolds number and Mach number conditions.

Detailed survey data at the blade exit showed the influence of secondary flows at positive incidence. The low momentum endwall flow was transported by the secondary flows to the suction side. As the incidence decreased, the blade row became unloaded and the secondary flows reduced. The flow field became largely two dimensional at this unloaded condition.

The blade loadings at different spanwise locations corroborated the two-dimensionality of the flowfield at the negative incidence condition. This test was run at low inlet turbulence levels in order to admit transitional flow on the blade surface. The measured loading reflected transitional flow on the blade suction surface. With the exception of the maximum Reynolds number condition, the loading diagrams were

consistent with a laminar separation, transition, and reattachment as a turbulent boundary layer. At the negative incidence angles, reverse loading was observed. Pressure surface separation was also noted at the extreme negative incidence angles.

The midspan surveys for all ten incidence angles were documented. The corresponding integrated losses showed that the loss levels decreased with increasing negative incidence until the pressure-side cove separation or reattachment occurred. Loss levels increased with decreasing Reynolds number as expected, and the range of acceptable loss levels decreased.

The results of this thesis show the effects of incidence and Reynolds number at a low inlet turbulence level. An additional test looking at the effects in a more engine-realistic high turbulence environment is warranted.

BIBLIOGRAPHY

[1] Johnson, W., Yamauchi, G. K., and Watts, M. E., "NASA Heavy Lift Rotorcraft Systems Investigation," NASA TP-2005-213467, Sep., 2005.

[2] Acree, C. W., Hyeonsoo, Y., and Sinsay, J. D., "Performance Optimization of the NASA Large Civil Tiltrotor," Proc. Int. Powered Lift Conf., London, UK, July 22-24, 2008.

[3] Stevens, M. A., Handschuh, R. F., Lewicki, D. G., "Variable/Multispeed Rotorcraft Drive System Concepts," NASA/TM–2009–215456; also ARL-TR-4728, Mar., 2009.

[4] D′Angelo, M., "Wide Speed Range Turboshaft Study," NASA/CR–1995–198380, Aug., 1995.

[5] Welch, G.E., "Assessment of Aerodynamic Challenges of a Variable-Speed Power Turbine for a Large Civil Tilt-Rotor Application," Proc. of the AHS Int. 66th Annual Forum, Arizona, May 2010; also NASA/TM-2010-216758.

[6] Snyder, C. A. and Thurman, D. R., Gas Turbine Characteristics for a Large Civil Tilt-Rotor (LCTR), Proc. AHS Int. 65th Ann. Forum, May, 2009.

[7] Hourmouziadis, J., "Aerodynamic Design of Low Pressure Turbines," in Blading Design for Axial Turbomachines, AGARD-LS-167, pp. 8-1 to 8-40, 1989.

[8] Haselbach, F., Schiffer, H.-P., Horsman, M., Dressen, S., Harvey, N., and Read, S., "The Application of Ultra High Lift Blading in the BR715 LP Turbine," *J. Turbomachinery*, 124, Jan 2002, pp. 45-51.

[9] Gier, J., Franke, M., Hübner, N. and Shröder, T., "Designing LP Turbines for Optimized Airfoil Lift," ASME-GT2008-51101, 2008.

[10] Halstead, D. E., Wisler, D. C., Okishii, T. H., Walker, G. J., Hodson, H. P, Shin, H-W., "Boundary Layer Development in Axial Compressors and Turbines: Part 3 of 4—LP Turbines," *J. Turbomachinery*, 119 (2), pp.225-237, April 1997.

[11] Coull, J. D., Thomas, R. L., Hodson, H. P., 2010, "Velocity Distributions for Low Pressure Turbines," *J. Turbomachinery*, 132, Oct, pp. 041006-1 – 13.

[12] Yamamoto, A. and Nouse, H., "Effects of Incidence on Three-Dimensional Flows in a Linear Turbine Cascade," 1988, *J. Turbomachinery,* 110 (4), Oct., pp. 486 (11 pages).

[13] Hodson, H.P. and Dominy, R.G., 1987b, "The Off-Design Performance of a Low-Pressure Turbine Cascade," *J. Turbomachinery,* 109, pp.201-209.

[14] Moustapha, S. H., Kacker, S. C., and Tremblay, B., 1990, "An improved incidence losses prediction method for turbine airfoils," *J. Turbomachinery*, 112, Apr., pp. 267-276.

[15] Jouini, D. B. M., Sjolander, S. A., and Moustapha, S. H., 2002 "Midspan Flow-Field Measurements for Two Transonic Linear Turbine Cascades at Off-Design Conditions," *J. Turbomachinery*, April, pp. 176-187. Vol. 124.

[16] Hoheisel H., Kiock, R., Lichtfuss, H. J., and Fottner, L., 1987, "Influence of free-stream turbulence and blade pressure gradient on boundary layer and loss behavior of turbine cascades," *J. Turbomachinery*, 109, April, pp. 210-219.

[17] Corriveau, D. and Sjolander, S. A., 2004, "Influence of Loading Distribution on the Performance of Transonic High Pressure Turbine Blades," *J. Turbomachinery*, Vol 126, Apr., pp.288-296.

[18] Verhoff, V. G., Camperchioli, W. P, and Lopez, I., 1992, "Transonic Turbine Blade Cascade Testing Facility", AIAA Paper No. 92-4034, NASA TM-105646.

[19] Giel, P.W., Sirbaugh, J.R, Lopez, I., and Van Fossen, G. J., 1996b, "Three Dimensional Navier Stokes Analysis and Redesign of an Imbedded Bellmouth Nozzle in a Turbine Cascade Inlet Section," *J. of Turbomachinery*, 118, No 3, pp 529-535. NASA/TM-107284 and U.S. Army ARL-MR-152.

[20] McVetta, A. B., Giel, P. W., and Welch, G. E., "Aerodynamic Investigation of Incidence Angle Effects in a Large Scale Transonic Turbine Cascade," AIAA-2012-3879, Atlanta, GA, Jul-Aug. 2012. NASA/TM—2013-218070.

[21] Giel, P.W., Thurman, D.R., Lopez, I., Boyle, R.J., Van Fossen, G.J., Jett T.A., Camperchioli, W.P., La, H., "Three Dimensional Flow Field Measurements in a Transonic Turbine Cascade," ASME 96-GT-113, 1996. Also NASA/TM-107388 and U.S. Army ARL-TR-1252.

[22] Giel, P. W., Bunker, R. S., VanFossen, G. J., and Boyle, R. J., 2000, "Heat Transfer Measurements and Predictions on a Power Generation Gas Turbine Blade," ASME 2000-GT-0209; Also NASA TM-2000-210021.

[23] Giel, P. W., Boyle, R. J., and Bunker, R. S., "Measurements and Predictions of Heat Transfer on Rotor Blades in a Transonic Turbine Cascade," *J. Turbomachinery*, 126 (1), pp. 110-121, Jan. 2004.

[24] Yavuzkurt, S., 1984, "A Guide to Uncertainty Analysis of Hot-Wire Data," Journal of Fluids Engineering, Vol. 106, pp. 181-186.

[25] Coull, J. D., Thomas, R. L., Hodson, H. P., 2010, "Velocity Distributions for Low Pressure Turbines," J. Turbomachinery, 132, Oct, pp. 041006-1 – 13.

[26] Ford, A, Bloxham, M., Turner, E., Clemens, E. and Gegg, S., "Design Optimization of Incidence-Tolerant Blading Relevant to Large Civil Tilt-Rotor Power Turbine Applications," NASA/CR—2012-217016, Dec. 2012.

[27] Ainley, D. G. and Mathieson, G. C. R., "A Method of Performance Estimation for Axial-Flow Turbines," Aeronautical Research Council (ARC), R&M 2974, 1957.